Banner appropriate to article type will appear here in typeset article

The Influence of Hypersonic Freestream Conicity on the Flow Over a Sphere

Sangdi Gu[1] †, Chih-Yung Wen[1], Jiaao Hao[1], Wentao Wang[2] and Qiu Wang[2]

[1]Department of Aeronautical and Aviation Engineering, The Hong Kong Polytechnic University, Kowloon, Hong Kong.

[2]State Key Laboratory of High Temperature Gas Dynamics, Institute of Mechanics, Chinese Academy of Sciences, No. 15 Beisihuanxi Road, Beijing, 100190, China.

(Received xx; revised xx; accepted xx)

The influence of freestream conicity on the various aspects of the flow over a spherical test model is examined using both analytical and numerical methods. For the analytical method, a simple closed-form analytical model is assembled. Six different freestream conditions with different Mach numbers, Reynolds numbers, and thermochemistry are tested at four different degrees of conicity corresponding to that which can realistically be encountered in experiments. It is found that the results around the stagnation point are mostly insensitive to the flow condition and gas type, except for some mild nonequilibrium effects, and excellent agreement between the analytical and numerical results exists. The shock stand-off distance on the stagnation streamline is shown to decrease with increasing conicity. This decrease increases the tangential velocity gradient at the stagnation point, increasing the stagnation point heat flux and decreasing the stagnation point boundary layer thickness. The freestream conicity is also found to alter the normalized distributions of the shock stand-off distance, heat flux, surface pressure, and boundary layer thickness with the angle from the stagnation point. In general, increasing the conicity magnifies the slope of these distributions. Regarding the boundary layer transition, it is found that if it occurs in a uniform freestream, it would also occur in a conical freestream, albeit with the transition point shifted upstream closer to the stagnation point due to the increase in the boundary layer edge tangential velocity. Overall, considering the relevant experimental uncertainties, corrections for freestream conicity are generally recommended when larger test models are used.

Key words:

1. Introduction

Experimental work in hypersonics is vital for progress in this field. This is enabled by impulse facilities, which produce hypersonic flow for a very short duration of time (Gu & Olivier 2020). An important component of impulse facilities is the nozzle which generates the hypersonic flow by converting thermal energy into kinetic energy via an expansion. The

† Email address for correspondence: sangdi.gu@polyu.edu.hk

Abstract must not spill onto p.2

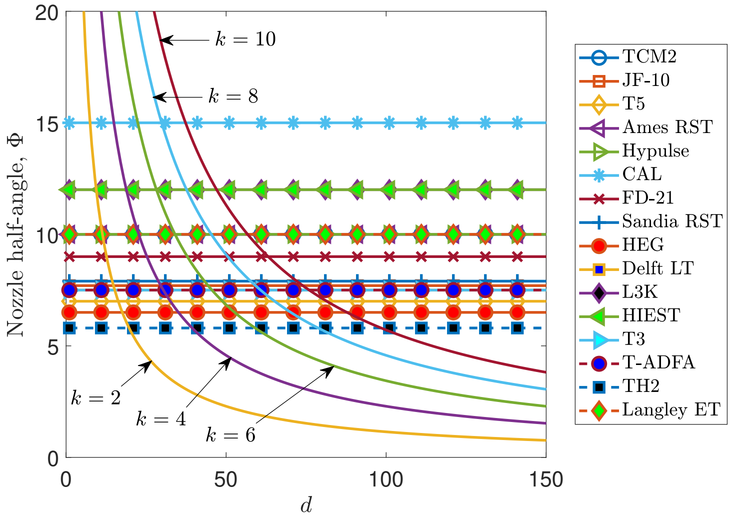

Figure 1: The relationship between the nozzle half-angle ϕ and the nonuniformity parameter d ($d = L_1/R_s$) for different values of k ($k = d\tan(\phi)$). Also shown are the ϕ values of the conical nozzle on TCM2 (Zeitoun *et al.* 1994), JF-10 (Zhao *et al.* 2005), T5 (Marineau & Hornung 2009), NASA Ames reflected shock tunnel (RST) (Menees 1972), Hypulse (Chue *et al.* 2003), Cornell Aeronautical Laboratory (CAL) RST (Hall & Russo 1966), FD-21 (Shen *et al.* 2023), Sandia RST (Lynch *et al.* 2023), HEG (Hannemann *et al.* 2018), DELFT Ludwieg tube (LT) (Schrijer & Bannink 2010), L3K (Gülhan *et al.* 2018), HIEST (Tanno & Itoh 2018), T3 (Mallinson *et al.* March 1996), T-ADFA (Krishna *et al.* 2018), TH2 (Gu *et al.* 2022), and NASA Langley expansion tunnel (ET) (Miller 1977).

nozzle is either contoured or conical. The contoured nozzle can produce uniform freestream (nozzle exit) conditions near the design condition, but may not work so well off-design. Also, the design procedure for these nozzles is non-trivial, especially for high-enthalpy conditions involving real-gas effects (Chan *et al.* 2018). On the other hand, the conical nozzle is easy to design and works over a wide range of conditions, but it produces a nonuniform (divergent) freestream. Nonetheless, the conical nozzle is still widely used due to its advantages; this is explicitly stated by Hornung (2019) and supported by figure 1 which lists the numerous facilities with a conical nozzle, corresponding to a large portion (around half) of all hypersonic impulse facilities in the world (Gu & Olivier 2020). Therefore, it is of significant interest to examine how the divergent freestream affects the experimentation.

The practical importance of studying the divergent freestream is in the interpretation and numerical reproduction of wind tunnel experiments. Recently, huge interest has been shown in understanding and better characterizing the test conditions generated in hypersonic impulse facilities because it is now acknowledged that this is crucial for improving the usefulness and quality of experimental work; in particular, much work has recently been done on determining the pressure, temperature, velocity, and chemical composition of the test conditions (Collen *et al.* 2022; Gu *et al.* 2022; Grossir *et al.* 2018; Jans *et al.* 2024; Finch *et al.* 2023). On the same theme is studying the influence of the freestream conicity. Interest in freestream conicity was shown decades ago (Lin *et al.* 1977; Golovachov 1985; Inouye 1966; Shapiro 1975; Lunev & Khramov 1970; Eremeitsev & Pilyugin 1981, 1984) but then forgotten about until it was revived recently by Hornung (2019) in line with the recent interest in characterizing test conditions. This revival is necessary as further work needs to be done in this area. The past works provide a good theoretical foundation for studying the problem but fail to relate to practical experimental conditions and arrangements, and lack a

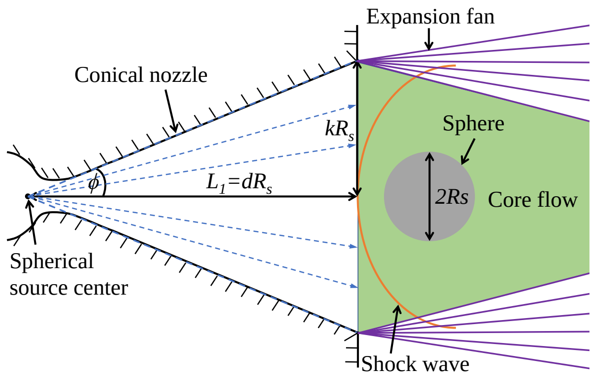

Figure 2: The schematic of the diverging freestream upstream of a spherical test model generated by a conical nozzle, which always operates in underexpanded mode in wind tunnels.

certain degree of comprehensiveness and systematization. Consequently, it remains largely unclear quantitatively how much the freestream conicity influences the experiments. This, subsequently, motivates the current work.

This paper will focus on the sphere being the experimental test model, which is commonly used for important fundamental studies, with its centre positioned on the nozzle centreline. The divergent freestream from a conical nozzle can be modelled as a steady spherical source flow (Hornung 2019; Lin *et al.* 1977; Golovachov 1985; Inouye 1966; Farokhi 2021), as shown in figure 2. One can define $d = L_1/R_s$, which measures the degree of nonuniformity, where R_s is the radius of the sphere and L_1 is the distance between the centre of the source and the shock wave on the axisymmetry axis; $d = \infty$ then corresponds to a uniform flow. The sphere is usually positioned near the nozzle exit such that the center of the shock front lies on the nozzle exit plane as shown in figure 2. In this case, the nozzle half-angle ϕ can be related to d via $\tan(\phi) = k/d$ where k is a measure of how big the spherical test model is relative to the nozzle exit: $k = 2$ would correspond to a large test model with a flowfield which roughly takes up all the core flow space while $k = 10$ would correspond to a small pitot or heat flux probe. The half-angle of the conical nozzles used on hypersonic impulse facilities, past and present, varies between 5.8° to 15° as shown in figure 1. Depending on the relative size of the test model (k), the degree of nonuniformity can realistically be around $d = 4 - 100$ in the experiments. More precisely, the d in practice will be slightly higher than this due to the boundary layer in the nozzle which generally reduces the effective nozzle half-angle from the geometric one reported in figure 1. Also, as mentioned earlier, the test model is normally placed near the nozzle exit where the core flow is largest (since wind tunnel nozzles are always underexpanded, the core flow gets smaller downstream due to the expansion fan originating from the wall corner at the nozzle exit as shown in figure 2). If, for whatever reason, the model is placed some distance downstream of the nozzle exit, the effect would be to increase ‘d’ (because L_1 is increased) and reduce the influence from freestream conicity. Additionally, if one really wanted to do this, it would probably be necessary to use a smaller model as well due to the reduced core flow, which will further increase ‘d’ (because R_s is decreased). Consequently, the lower bound of $d = 4$ stated above can duly be considered a conservative estimate of the maximum influence from freestream conicity that may be encountered in practice.

In this paper, we will examine how much effect this nonuniformity can have on the various aspects of the flow over the spherical test model on the forebody—such as the shock wave, pressure, heat flux, boundary layer, and tangential velocity gradient—under different flow conditions and gas states. Both analytical and numerical methods will be used, and the results between the two will be compared. The numerical work will include thermochemical nonequilibrium simulations; this is unlike the previous studies that examine the influence of freestream conicity, which only consider perfect gas or equilibrium flows (Lin *et al.* 1977; Golovachov 1985; Inouye 1966; Shapiro 1975; Hornung 2019; Lunev & Khramov 1970; Eremeitsev & Pilyugin 1981, 1984). Also unlike the previous works, the results here will be fully related to practical experimental scenarios by considering the realistic range of 'd' and by considering the uncertainties (measurement uncertainties and shot-to-shot variations) of hypersonic experiments. In addition to answering the aforementioned important question of just how much the freestream conicity influences the experiments, the underlying physics involved will be thoroughly explained as well, which is not discussed in many of the earlier works which mostly only look to predict and quantify the influence of freestream conicity without really attempting to provide a physical explanation for the observations.

2. Methodology

2.1. *Analytical Method*

An appreciable amount of theoretical work exists in literature (mostly done by Russian researchers during the 1970s and 1980s) to describe the influence of hypersonic freestream conicity on the flow over a sphere. In these studies, analytical equations have been derived which predict how much effect a divergent freestream has on the various aspects of the flow over a spherical test model. More precisely, these works compare conical freestreams with the equivalent uniform freestreams where the freestream properties immediately ahead of the shock on the symmetry axis are identical. From these past studies, a comprehensive analytical model is subsequently compiled for use in the current work which is described as follows, aided by figures 3 and 4.

To quantify the influence of the freestream conicity on the shock stand-off distance on the symmetry axis, Shapiro (1975) gave

$$\frac{\Delta^0}{\Delta^0_\infty} = \frac{\theta^s}{\theta^s_\infty}\frac{1}{1+\Delta^0_\infty(1-\frac{\theta^s}{\theta^s_\infty})} \tag{2.1}$$

where Δ^0 and Δ^0_∞ are the shock stand-off distances on the symmetry axis for a nonuniform and uniform freestream, respectively, and

$$\frac{\theta^s}{\theta^s_\infty} = \frac{1}{2}\left[\left(\frac{1+\Delta^0_\infty}{\Delta^0_\infty}+1\right)-\sqrt{\left(\frac{1+\Delta^0_\infty}{\Delta^0_\infty}-1\right)^2+\frac{4}{l}\frac{1+\Delta^0_\infty}{\Delta^0_\infty}}\right] \tag{2.2}$$

where θ^s and θ^s_∞ are the locations (angle from the symmetry axis) of the sonic point on the boundary layer edge (or surface of the sphere for inviscid flows) for a nonuniform and uniform freestream, respectively, and l is the distance between the centre of the source and centre of the sphere. The above equations were derived, without needing to define any gas properties, based on geometric considerations of the shock wave, sphere, and conical freestream, and assuming the normalized distribution of the shock standoff distance, Δ/Δ^0, is independent of the degree of freestream conicity when given as a function of $\eta = \theta/\theta^s$ instead of θ (that is, θ is normalized with that of the sonic point). The above equations, along with the assumption of Δ/Δ^0 being a universal function of η, are shown by Shapiro (1975) and Golovachov (1985) to work well after comparing with both viscous and inviscid CFD simulations for a range of Mach numbers $(3-10)$, Reynolds numbers $(177-35500)$, and d $(0.3-25)$ for both

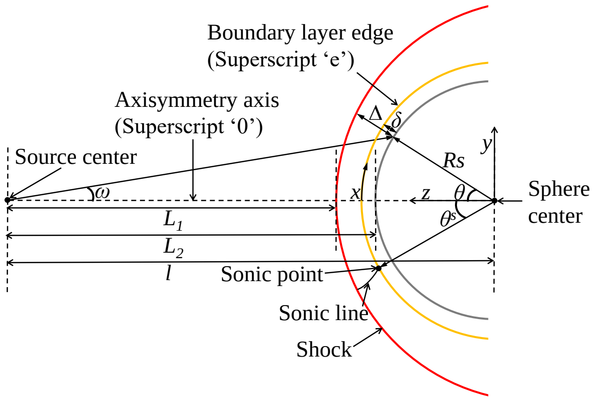

Figure 3: Flowfield around a sphere in a conical freestream with the nomenclatures.

perfect gas and equilibrium flows. The above equations require Δ_∞^0 as a priori, which can be calculated analytically with (Lobb 1964)

$$\Delta_\infty^0 = 0.82 R_s \frac{\rho_1}{\rho_2} \tag{2.3}$$

where ρ_1 and ρ_2 are the flow densities before and after the shock on the symmetry axis, respectively. This correlation is obtained based on the numerical results of Van Dyke (1958) for a perfect gas for Mach numbers between 1.5 and 10.

Recently, Hornung (2019) independently derived another expression describing the influence of the freestream conicity on the shock stand-off distance on the symmetry axis based on a control volume conservation of mass argument with geometric relations, without needing to specify any gas properties, while assuming the shock-parallel component of velocity is constant across the shock layer. Further assuming the average density across the shock layer remains constant with varying freestream conicity, which is true for perfect gas or equilibrium flows, one can derive

$$\frac{\Delta^0}{\Delta_\infty^0} = \frac{1}{1 + \frac{(R_c^0)_\infty}{L_1}} \tag{2.4}$$

where $\left(R_c^0\right)_\infty$ is the radius of curvature of the shock on the symmetry axis in a uniform freestream, which can be calculated analytically with the semi-empirical correlation of Billig (1967) for a perfect gas with $\gamma = 1.4$

$$\left(R_c^0\right)_\infty = 1.143 \exp\left(\frac{0.54}{(M-1)^{1.2}}\right) R_s \tag{2.5}$$

where M is the freestream Mach number.

To describe the influence of the freestream conicity on the stagnation point heat flux, Eremeitsev & Pilyugin (1981) gave

$$\frac{q^0}{q_\infty^0} = \sqrt{1 + \frac{R_s}{L_2}} \tag{2.6}$$

where L_2 is the distance between the centre of the source and the stagnation point on the sphere ($L_2 = L_1 + \Delta^0$). This equation is derived, without considering finite-rate thermochemistry, based on the self-similar boundary layer theory of Lees (1956) with the boundary layer edge

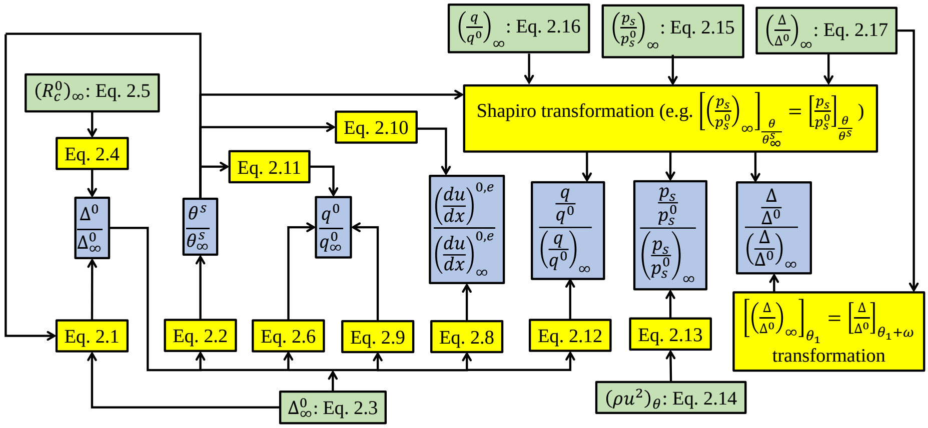

Figure 4: Flowchart describing the operation of the analytical model. The blue boxes are the parameters to be predicted, the yellow boxes are the predictors, and the green boxes are the inputs (other than trivial freestream values) to the predictors.

conditions obtained using thin shock-layer theory where $M_\infty \to \infty$ and $\gamma_\infty \to 1$. In such a limit, the wall-normal gradient of the flow properties is assumed to be large compared with their tangential gradient, and the shock shape, the body shape, and the streamline shapes are assumed to be all the same. Analytical expressions for the boundary layer edge properties are obtained, according to the method of Chernyi (1961), by replacing the flow variables in the von Mises formulation of the governing equations by their power series expansion truncated after the first term, which is then used with Lees' theory to obtain equation 2.6. As suggested by this equation, the gas model dependent terms disappear indicating q^0/q_∞^0 can be predicted without specifying any gas properties.

An alternative expression for q^0/q_∞^0 can be derived as follows. Because the freestream conicity does not change the flow properties at the stagnation point—such as the pressure, density, temperature, and enthalpy—for a perfect or equilibrium gas (Golovachov 1985; Shapiro 1975), the change in the stagnation point heat flux, in this case, comes purely from the change in the tangential velocity gradient at the boundary layer edge on the stagnation streamline, $(du/dx)^{0,e}$, according to Fay & Riddell (1958) with

$$q^0 \propto \sqrt{\left(\frac{du}{dx}\right)^{0,e}} \tag{2.7}$$

assuming a perfect or equilibrium gas. Following from Olivier (1995) who obtained an analytical expression for the tangential velocity gradient after an integral method is used to solve the two-dimensional conservation equations for the stagnation point without needing to specify any gas properties, the tangential velocity gradient assuming a perfect or equilibrium gas can be derived as

$$\left(\frac{du}{dx}\right)^{0,e} \propto \frac{R_s + \Delta^0}{\Delta^0} \tag{2.8}$$

Therefore, one can write

$$\frac{q^0}{q^0_\infty} = \sqrt{\frac{R_s + \Delta^0}{\frac{\Delta^0}{\Delta^0_\infty} R_s + \Delta^0}} \tag{2.9}$$

Alternatively, Shapiro (1975) proposed another expression for predicting the influence of freestream conicity on the tangential velocity gradient given as

$$\frac{\left(\frac{du}{dx}\right)^{0,e}}{\left(\frac{du}{dx}\right)^{0,e}_\infty} = \frac{\theta^s_\infty}{\theta^s} \tag{2.10}$$

which is simply derived assuming the tangential velocity gradient remains constant along the boundary layer edge between the axisymmetry axis and the sonic point. Combining equations 2.7 and 2.10 gives

$$\frac{q^0}{q^0_\infty} = \sqrt{\frac{\theta^s_\infty}{\theta^s}} \tag{2.11}$$

Analytical methods also exist to describe the influence of the freestream conicity on the flow property distributions in the flow around the sphere. For the normalized surface heat flux distribution, Eremeitsev & Pilyugin (1984) gave, based on a similar method they used in their previous work (Eremeitsev & Pilyugin 1981) discussed above involving thin shock-layer and self-similar boundary layer theories,

$$\frac{\frac{q}{q^0}}{\left(\frac{q}{q^0}\right)_\infty} = [\cos(\theta)]^{\frac{R_s}{3L_2}\left(\frac{5R_s}{L_2}+8\right)} \tag{2.12}$$

where θ is the angle from the symmetry axis of some point on the sphere surface, and q/q^0 is the normalized heat flux (normalized by the value at the stagnation point). Subscript ∞ indicates the uniform freestream result as usual. Again, finite-rate thermochemistry is not considered in the derivation, and the gas property dependent terms disappear.

For the normalized surface pressure distribution, Lunev & Khramov (1970) gave, based on the classic Newtonian theory for spheres and accounting for the conically expanding freestream,

$$\frac{\frac{p_s}{p^0_s}}{\left(\frac{p_s}{p^0_s}\right)_\infty} = \frac{\left(\rho u^2\right)_\theta}{\left(\rho u^2\right)_{\theta=0}} \frac{\cos^2(\omega + \theta)}{\cos^2(\theta)} \tag{2.13}$$

where ω is the flow divergence angle at θ, p_s/p^0_s is the normalized surface pressure (normalized by the pitot pressure), and $\left(\rho u^2\right)_\theta$ is the local ram pressure on the sphere surface, assuming an ideal Newtonian flow, at θ. $\left(\rho u^2\right)_\theta$ at different locations can be calculated from the governing equations for a steady spherical source flow in closed-form which, for a perfect gas, is (Golovachov 1985)

$$
\begin{aligned}
U &= \left(\frac{r^*}{r}\right)^2 \left(\frac{2}{\gamma+1}\right)^{\frac{1}{\gamma-1}} \left(1 - \frac{\gamma-1}{\gamma+1}U^2\right)^{-\frac{1}{\gamma-1}} \\
\frac{p}{p^*} &= \left(\frac{r^*}{r}\right)^2 \left(1 - \frac{\gamma-1}{\gamma+1}U^2\right) \left(\frac{\gamma+1}{2U}\right) \\
\frac{\rho}{\rho^*} &= \left(\frac{r^*}{r}\right)^2 \left(\frac{1}{U}\right)
\end{aligned}
\tag{2.14}
$$

where γ, p, ρ, and $U = u/u^*$ are the heat capacity ratio, static pressure, density, and normalized value of the velocity u in the source flow at a distance of r from the source center. The superscript '$*$' values represent the properties at r^* where $u = u^* = \sqrt{\gamma p^*/\rho^*}$ ($M = 1$). Newtonian theory is essentially a pure fluid mechanics theory and does not consider thermodynamics, which makes it suitable for pressure predictions since pressure behind a strong shock wave is only weakly dependent on the thermodynamics (Chernyi 1961; Anderson 2019).

Furthermore, Shapiro (1975) proposed a transformation, where the distribution is given in terms of $\eta = \theta/\theta^s$ instead of θ, allowing all the results (nonuniform and uniform) to coalesce, as mentioned earlier in this section. In other words, the distributions become independent of the degree of freestream conicity when the distributions are considered functions of η. This transformation, discovered via analysis of numerous numerical simulations, is suggested to work not only on the shock stand-off distance distribution, but also on the surface pressure and heat flux distributions regardless of the gas type for both frozen and equilibrium flows (Golovachov 1985; Shapiro 1975). With this transformation, one can obtain the distributions in some nonuniform freestream given the corresponding distribution in the equivalent uniform freestream and the sonic point ratio θ^s/θ^s_∞ are known. For a uniform freestream, the normalized pressure distribution can be obtained analytically from Newtonian flow theory (Anderson 2019)

$$
\left(\frac{p_s}{p_s^0}\right)_\infty = \cos^2(\theta) \tag{2.15}
$$

which works for any hypersonic flow. The normalized heat flux distribution can be obtained analytically from (Murzinov 1966)

$$
\left(\frac{q}{q^0}\right)_\infty = 0.55 + 0.45cos(2\theta) \tag{2.16}
$$

which is correlated from numerous equilibrium simulations, but is shown to also work well for both non-reacting (Wang *et al.* 2010; Gu *et al.* 2022) and nonequilibrium (Voronkin & Geraskina 1969) simulations. The normalized shock stand-off distance distribution can be obtained analytically from the semi-empirical correlation of Billig (1967),

$$
\begin{gathered}
\left(\frac{\Delta}{\Delta^0}\right)_\infty = \frac{\sqrt{z^2+y^2} - R_s}{\Delta^0_\infty} \\
\theta = \tan^{-1}\left(\frac{y}{z}\right) \\
z = R_s + \Delta^0_\infty - \left(R_c^0\right)_\infty \cot^2\left(\sin^{-1}\left(\frac{1}{M}\right)\right) \left[\sqrt{1 + \frac{y^2\tan^2(\sin^{-1}(\frac{1}{M}))}{\left(R_c^0\right)^2_\infty}} - 1\right]
\end{gathered}
\tag{2.17}
$$

who assumed the shock shape is a hyperbola that asymptotes to the freestream Mach angle, which is a good approximation for the shock over a sphere in any hypersonic flow (Zander *et al.* 2014; Hornung 2010).

For predicting the influence of freestream conicity on the normalized shock stand-off distance distribution, an alternative transformation may be proposed in which all the results (nonuniform and uniform) are assumed to coalesce when the distribution is given in terms of $\theta + \omega$ (where ω is the flow divergence angle at θ, defined earlier in this section) instead of θ. That is, it assumes that the normalized shock stand-off distance at some $\theta = \theta_1$ in a uniform flow is equal to that at $\theta = \theta_1 - \omega$ in a nonuniform flow.

Overall, the analytical model is summarized in figure 4, which can be used to accurately predict (shown later in this paper) the influence of freestream conicity on various aspects of the flow over a sphere. This analytical model is formed by different analytical equations which are used together to make the predictions without needing any input from CFD (Computational Fluid Dynamics). Although, many of these equations in our analytical model are derived by others (except equations 2.9 and 2.11, and the transformation of the normalized shock standoff distance distribution, which are our own contributions), using these analytical equations together in the way described in figure 4 is an important original contribution of the current work. For example, Shapiro's transformation requires the corresponding distribution in a uniform freestream as an input, which is originally obtained from CFD (Shapiro 1975; Golovachov 1985; Golovachev & Leont'eva 1983) but we propose the use of analytical expressions for this in our model allowing for a more practical, fully analytical way of determining the influence from freestream conicity. Similar can be said for many of the other equations in our analytical model. Therefore, aside from bringing together relevant equations that have been scattered throughout the literature and providing original commentaries regarding the derivation and limitations of these analytical expressions, a methodology is given for using these equations together to accurately predict the influence of freestream conicity without needing any input from CFD. Furthermore, the compilation and subsequent visual description of the model shown in figure 4 allows us to also gain insight into the relationship among how the different parameters are influenced by the freestream conicity. From this, it can be seen that θ^s/θ^s_∞ is the most fundamental parameter characterizing the influence from the freestream conicity which can be related to every other parameter.

Most of the predictors for the influence of freestream conicity (yellow boxes in figure 4) used as part of our analytical model have never been compared with CFD before (e.g. equations 2.1, 2.8, 2.10, 2.9, 2.11, 2.12, 2.13). Even for the equations that have been compared to CFD before, most of them have not been compared to modern-day CFD results (e.g. equations 2.2, 2.6, Shapiro's transformation); the older CFD simulations that were compared to are less accurate as they either first solved the Euler equations to get the inviscid flowfield which is then used as the boundary layer edge condition to solve the boundary layer equations (Golovachov 1985), or used very few grids (e.g. 7 x 26 in the tangential and wall-normal directions, respectively) when solving the Navier-Stokes equations (Golovachev & Leont'eva 1983). Therefore, it is not immediately clear whether our analytical model could give accurate enough results, and a systematic validation is, thus, required to find out. As will be presented later in this paper, good agreement is observed between our analytical model and CFD for a range of flow conditions (different Mach and Reynolds numbers, and gas models), which is a non-trivial and important result. Furthermore, the results of this comparison when considered together with how the analytical equations were derived allow further insights to be revealed regarding the physical problem.

None of the equations given above in this section explicitly consider thermochemical nonequilibrium effects in their derivation (which is expected considering there are rarely analytical solutions when finite-rate thermochemistry is involved). However, this is not an issue because, as will be shown later on in this paper, the influence of freestream conicity is mostly insensitive to nonequilibrium effects. This may be expected considering Shapiro (1975) and Golovachov (1985) have shown that the influence of freestream conicity is mostly independent of the flow condition, type of gas, and whether the gas is in equilibrium or frozen; the same can be deduced from the derivations of Hornung (2019); Lunev & Khramov (1970); Eremeitsev & Pilyugin (1981, 1984) who demonstrated that it may be unnecessary to specify the thermodynamic properties of the gas when predicting the influence of freestream conicity, as mentioned above. Thus, it is found that good predictions of the influence of freestream conicity are made by the current analytical model even when the flow is in thermochemical nonequilibrium.

2.2. *Numerical Method*

The Navier-Stokes solver 'Eilmer' from The University of Queensland is used for the current work. As shown by Gollan & Jacobs (2013) and Gibbons *et al.* (2023), Eilmer is a validated and established tool for the simulation of various hypersonic flows, including frozen (perfect gas), thermochemical equilibrium, and thermochemical nonequilibrium flows. Accurate predictions of the flowfield and wall heat flux in such conditions are demonstrated by comparing them to experimental measurements (Park *et al.* 2016; Jacobs *et al.* 2015; Deepak *et al.* 2012). Due to the reliability of the code, it has been used as a validation tool for new models of high-enthalpy blunt body viscous flows (Gu *et al.* 2022; Ewenz Rocher *et al.* 2021; Yang & Park 2019).

Eilmer is an open-source explicit Navier–Stokes solver for transient compressible flow in two and three dimensions based on the integral form of the Navier-Stokes equations. The core gas dynamics formulation is based on finite-volume cells. The inviscid fluxes are calculated at the cell interfaces using an adaptive flux calculator in which the Harten-Lax-vanLeer-Einfeldt (HLLE) scheme (Einfeldt 1988) is applied near shocks and the Roe scheme (Roe 1981) is applied elsewhere; as discussed by Nishikawa & Kitamura (2008), this resolves the problem of simulating flowfields containing flow features that require low dissipation schemes to accurately capture but also containing discontinuities which require high dissipation schemes to avoid numerical instabilities (e.g. the carbuncle problem). The viscous fluxes are calculated using the averaged values of the viscous stresses at the cell vertices. A modified van Albada limiter (van Albada *et al.* 1997) and a Monotonic Upstream-centred Scheme for Conservation Laws (van Leer 1979) reconstruction scheme are used to obtain second-order spatial accuracy. The time advancement procedure is based on the operator-splitting method (Oran & Boris 2001) and the time integration uses the implicit first-order Runge-Kutta method (Petzold 1986). Numerical stability is maintained by the Courant–Friedrichs–Lewy (CFL) criterion, with a CFL value of 0.5 used in the current work. For thermochemical nonequilibrium simulations, Park's two-temperature model (Park 1993) is used in which the dissociation/recombination reactions are controlled by an effective temperature, T_c, given as $T_c = T_{tr}^{0.5} T_v^{0.5}$ where T_{tr} is the translational-rotational temperature and T_v is the vibrational temperature. The thermochemical effects are handled with specialised updating schemes that are coupled into the overall time-stepping scheme. The species mass diffusion is modelled using Fick's first law assuming binary diffusion (Anderson 2019). The heat flux for thermochemical nonequilibrium flows is calculated via the formulation given by Gupta *et al.* (1990). The reader is referred to Gollan & Jacobs (2013); Gibbons *et al.* (2023); Jacobs *et al.* (2010) for further details on Eilmer, including its formulation and validation. The current work makes use of the existing features of the code without any further development.

The numerical test conditions are shown in table 1. Conditions 1-4 originate from a reservoir pressure and temperature of 2 MPa and 800 K, respectively, which are representative of conditions in a cold hypersonic (low-enthalpy) facility (Schrijer & Bannink 2010).

Condition	Gas Model	R_s, m	p_∞, Pa	T_∞, K	u_∞, m/s	M_∞	Re
1	PG	0.01	3780.0	133.33	1157.4	5.0	1.24×10^5
2	PG	0.01	204.8	57.97	1221.1	8.0	3.93×10^4
3	PG	0.1	204.8	57.97	1221.1	8.0	3.93×10^5
4	PG	0.01	24.9	31.75	1242.5	11.0	1.85×10^4
5	NONEQ	0.01	701.0	723.0	4842.0	8.7	4.61×10^3
6	EQ	0.01	701.0	723.0	4842.0	9.0	4.79×10^3

Table 1: The numerical test conditions. 'PG', 'EQ', and 'NONEQ' refer to perfect gas, thermochemical equilibrium, and thermochemical nonequilibrium simulations, respectively. p_∞, T_∞, u_∞, and M_∞ are the freestream static pressure, temperature, velocity, and Mach number. The Reynolds number, Re, is calculated using the freestream properties and R_s.

Condition 3 is the same as condition 2 except the sphere is larger. Condition 5 is a high-enthalpy condition corresponding to the HEG Condition H12R0.39 (Shen *et al.* 2023; Hannemann *et al.* 2018). Condition 6 is the same as Condition 5 except thermochemical equilibrium is assumed. The freestream chemical composition (mass fraction) in the perfect gas and equilibrium simulations is N_2 = 0.767 and O_2 = 0.233, while that in Condition 5 (the nonequilibrium simulation) is N_2 = 0.7417, N = 0.0, O_2 = 0.1634, O=0.0454, and NO = 0.0495. Condition 5 has a freestream vibrational temperature of 2300 K. Although variants of air are explicitly used as the test gas here, the results presented later in this paper are not limited to this gas because the influence of freestream conicity is mostly insensitive to the flow condition and type of gas as have been shown (Shapiro 1975; Golovachov 1985; Lunev & Khramov 1970; Hornung 2019; Eremeitsev & Pilyugin 1981, 1984) for some properties in the flow over a sphere and will be further demonstrated later in this paper for some more properties, considering PG air and EQ air are essentially different types of gas with totally different species composition.

The computational domain and the boundary conditions used for the current work are shown in figure 5. The simulation is two-dimensional axisymmetric, which is enough for the intents and purposes of the current work (three-dimensional simulations of such flows are known to be very difficult and contain significant numerical error as discussed by Candler *et al.* (2007); therefore, there is really not much to be gained and a lot to be lost if one chooses to compute in three dimensions for the current work).

For Condition 5, both a non-catalytic (NC, where no catalytic interaction occurs between gas and surface) and super-catalytic (SC, where instantaneous equilibration of the gas occurs at the surface) wall are tested, which correspond to surface reaction Damköhler numbers of 0 and ∞, respectively (Inger 1963). Relating to real applicability, an NC wall would correspond to some glass surface while an SC wall would correspond to some metallic surface (Goulard 1958). The surface catalycity is really only relevant for thermochemical nonequilibrium simulations. For perfect gas simulations, the chemical composition in the fluid remains a perfect air mixture (mass fractions of N_2 = 0.767 and O_2 = 0.233); therefore, nothing can happen at the wall due to surface catalycity since the chemical composition of the fluid at the wall is already in equilibrium at the corresponding wall temperature (295 K). Likewise, for equilibrium simulations, the local chemical composition of the fluid is always in equilibrium at the local temperature; therefore, the fluid at the wall is also in equilibrium at the corresponding wall temperature which means that surface catalycity cannot have any

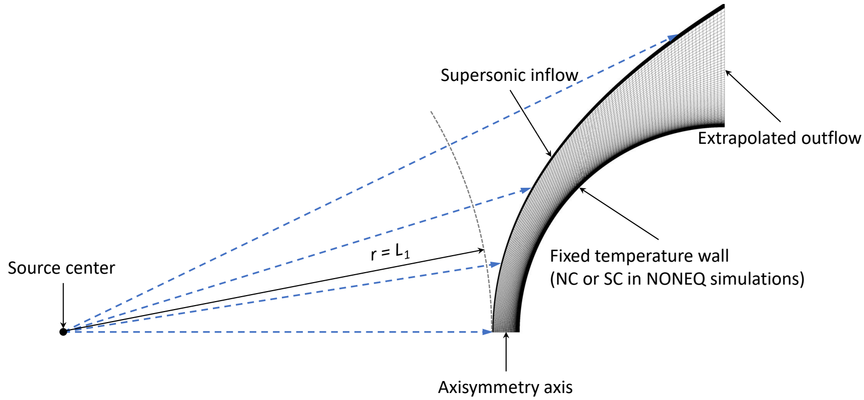

Figure 5: The computational domain, boundary conditions, and mesh. The wall temperature T^w is fixed at 295 K.

influence here. Consequently, surface catalycity can only impact nonequilibrium simulations (e.g. Condition 5 in the current work).

The inflow boundary is made to be adaptive and fit with the shock front. The freestream conditions shown in table 1 correspond to that of the uniform freestream which in turn corresponds to the freestream condition immediately ahead of the shock on the symmetry axis in the case of a nonuniform freestream ($r = L_1$ in figure 5) which is modelled as a spherical source flow. Subsequently, for the nonuniform freestream simulations, the flow state on the inflow faces has to be computed from the governing equations of a steady spherical source flow in differential form in spherical coordinates given as (Crittenden & Balachandar 2018),

$$\begin{aligned} \partial\left(r^2 \rho u_r\right) &= 0 \\ \partial p + \rho u_r \partial u_r &= 0 \\ \partial h + u_r \partial u_r &= 0 \end{aligned} \tag{2.18}$$

where h is the specific enthalpy and u_r is the radial velocity. The solution is numerically obtained with the equation of state after specifying the location of the source centre and the flow condition at some specific distance of r from the source centre. Different locations for the source centre are tested such that d = 4, 25, and 100 are examined for each condition in table 1. We specify the flow condition at $r = L_1$, which is given in table 1, and the flow state on the inflow faces is computed according to equation 2.18 as mentioned above. A frozen source flow is assumed for Conditions 1-5 while an equilibrium source flow is assumed for Condition 6.

A structured grid of 240×240 is used, which is similar to that used in other comparable works from recent literature (Fahy *et al.* 2021; Luo *et al.* 2023; Guo *et al.* 2024). Strong clustering is implemented at the shock front and normal to the wall, as shown in figure 5. The clustering at the shock front is regular with a spacing of around $0.5 - 2.0$ μm while the clustering normal to the wall decreases in the radial direction with a minimum cell spacing of around $0.05 - 1.0$ μm at the first cell from the wall at the stagnation point, depending on the condition. Mild clustering is made in the wall-tangential direction towards the axisymmetry axis, as shown in figure 5. The minimum spacing in the tangential direction, which is found on the first cell from the axisymmetry axis, is around 10 μm. The average spacing in the wall-normal and wall-tangential directions is around 15 μm and 85 μm, respectively.

For predicting the surface heat flux, various computational scientists have stated that the

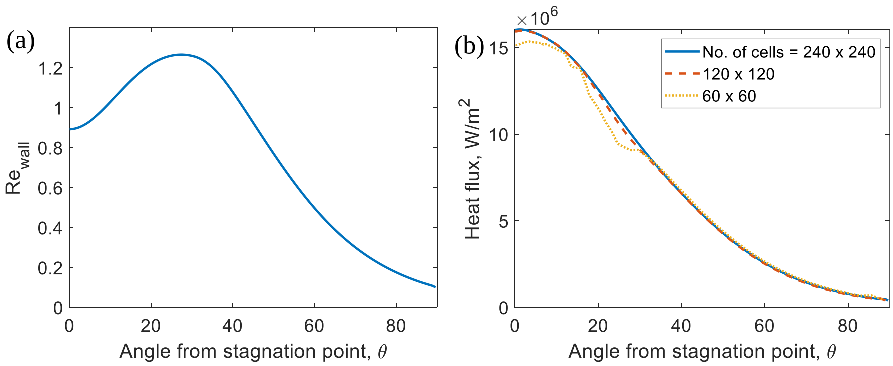

Figure 6: The wall (a) cell Reynolds number and (b) heat flux for Condition 5 (NONEQ) with a nonuniform freestream of d = 4 and a non-catalytic wall. The angle is in degrees.

wall cell Reynolds number, Re_{wall}, needs to be below a certain value. Some authors state that any Re_{wall} value below 3 would give good results (Papadopoulos *et al.* 1999), while other authors state that the Re_{wall} value should be around 1 (Ren *et al.* 2019). The latter condition is achieved for the current work using a 240 × 240 grid for all the simulated cases as shown exemplarily in figure 6 (a) for Condition 5. A mesh independence study is carried out for each test case by testing with scaled meshes and comparing the heat flux distribution around the sphere which is influenced by many aspects of the flowfield and is the most grid-sensitive parameter (Candler *et al.* 2007; Mazaheri & Kleb 2007; Kitamura *et al.* 2010; Gu *et al.* 2022). An example is shown in figure 6 (b) for Condition 5; the result is essentially converged when more than 120 × 120 cells are used, and similarly for the other test cases. Therefore, all the numerical results presented in the subsequent sections, which are obtained using a 240 × 240 grid, are converged. An estimated representative uncertainty of less than ±0.5 % can be given to the computed stagnation point heat flux (Gu *et al.* 2022), which is already the most uncertain property calculated in these kinds of simulations (Capriati *et al.* 2022). Hence, the numerical uncertainties of the current simulations can be considered negligible for the intent and purposes of the current work. Further validation of these numerical results is implied from the excellent agreement with the analytical/theoretical results, as will be shown below in section 4.

3. Experimental Uncertainties

Before presenting the results examining the influence of freestream conicity on the flow over a sphere, it is necessary to first define the representative experimental uncertainties for the flow properties of interest. This work is essential because the importance of freestream conicity must later be interpreted in relation to the experimental uncertainties (e.g. if the influence of freestream conicity is small relative to the experimental uncertainties, then one may suggest that freestream conicity is unimportant, and vice versa). The uncertainties are summarized in table 2. The total uncertainty is considered the sum of the measurement uncertainty, which is the uncertainty originating from the measurement-taking device/method, and the test condition repeatability, which is the uncertainty originating from the facility generating a slightly different test condition in each shot.

For the shock stand-off distance, Δ, measured via imaging, the measurement uncertainty reported in the literature ranges from about 5 % to 10 % (Sudhiesh Kumar & Reddy 2016; Zander *et al.* 2014). Assuming that the total uncertainty is manifested as the shot-

Uncertainty Type	Δ	q	Δ/Δ^0	q/q^0	p_s/p_s^0
Measurement uncertainty, %	±5-10	±5-10	±10-20	±10-20	±6-12
Test condition repeatability, %	±5-10	±15-20	0	0	0
Total uncertainty, %	±15	±20-30	±10-20	±10-20	±6-12

Table 2: Representative experimental uncertainties.

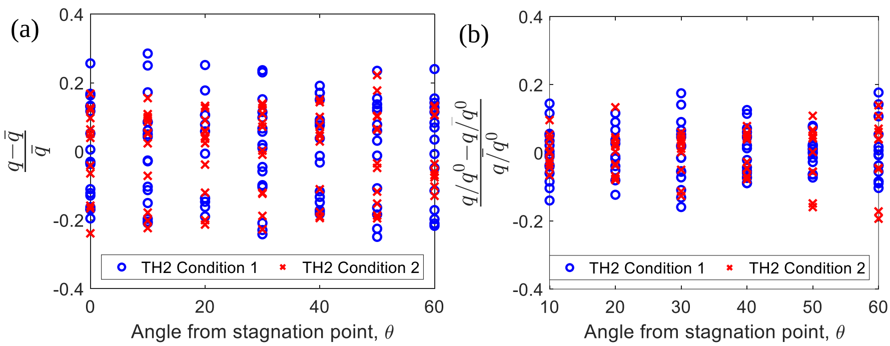

Figure 7: The relative shot-to-shot and mirror measurement variation of (a) the absolute heat flux measurements, and (b) the normalized heat flux measurements, on a 39 mm diameter sphere. The upper-bar symbol denotes the average value. The angle is in degrees.

to-shot variation of repeated measurements of Δ at a given nominal test condition, this is reported to be around 15 % (Zander *et al.* 2014). Consequently, the contribution to the total uncertainty from the test condition repeatability is around 5-10 %. For the surface heat flux, the measurement uncertainty of measurements made using coaxial thermocouples is reported to be around 5-10 % (Park *et al.* 2021). The shot-to-shot variation of coaxial thermocouple heat flux measurements made at various locations on the surface of a 39 mm diameter sphere in the TH2 reflected shock tunnel at two different test conditions (Gu *et al.* 2022) is presented in figure 7 (a). Also included in the figure, and treated as shot-to-shot variations, are measurements made in the same shot at the same angle from the stagnation point but at opposite locations on the sphere (mirror measurements). Independent of the angle from the stagnation point, the results indicate a total uncertainty of around 20-30 %, which is also consistent with the data in (Rose & Stark 1958; Eitelberg *et al.* 1996), with the test condition repeatability contributing about 15-20 %.

The normalized heat flux, q/q^0, and surface pressure, p/p^0, distributions are known to be rather insensitive to the freestream condition (and the type of gas) (Lees 1956; Murzinov 1966; Anderson 2019). The same is found for the normalized shock stand-off distance distribution, Δ/Δ^0, as shown in figure 8, obtained using equation 2.17; although this equation still contains the Mach number, shock standoff distance, and shock radius of curvature, which are freestream dependent quantities (unlike the equations for q/q^0 and p/p^0 which contain no such quantities), their influence on the result is rather weak. Therefore, the test condition repeatability will not contribute to the total uncertainty for these normalized distribution measurements. The total uncertainty would then be just the measurement uncertainty which, for these normalized measurements, would be two times the measurement uncertainty of the absolute measurements since these normalized measurements are obtained as a quotient of two absolute measurements. This results in total uncertainties of around ±10-20 % for

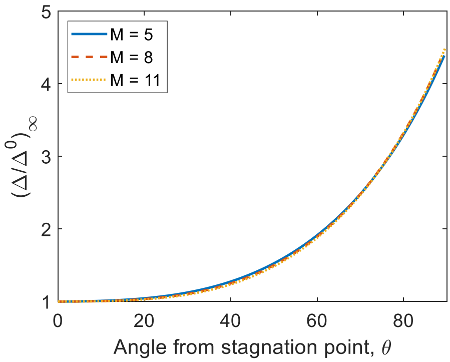

Figure 8: The normalized shock stand-off distance distribution obtained using equation 2.17. The angle is in degrees.

the normalized shock stand-off distance and heat flux measurements, and ±6-12 % for the normalized surface pressure measurements.

For the normalized surface pressure and heat flux uncertainties estimated here, experimental data are available for comparison. Shot-to-shot and mirror measurement scatters of the normalized surface pressure are reported by Karl *et al.* (2003) and Rose & Stark (1958); variations of around ±5-10 % are observed which is consistent with the estimated uncertainty in table 2. Shot-to-shot and mirror measurement scatters of the normalized heat flux taken in TH2 are shown in figure 7 (b); independent of the angle from the stagnation point, variations of around ±10-20 % are observed which is exactly consistent with the estimated value in table 2. The experimental data reported by Karl *et al.* (2003) and Eitelberg *et al.* (1996) show further consistency. Also, the scatter of the normalized values in figure 7 (b) is distinctly smaller than that of the absolute values in figure 7 (a) providing further confirmation of the role of the test condition repeatability discussed earlier. As shown in table 2, the test condition repeatability contributes significantly to the total uncertainty of Δ and q measurements. Therefore, as a corollary, instead of interpreting and analysing experimental data by simply using a nominal estimate of the test condition, it is of significant benefit to obtain a unique freestream estimate for each individual shot, using the method of Gu *et al.* (2022) for example, to eliminate the uncertainty contribution from the test condition repeatability.

4. Results

4.1. *Point Properties*

The influence of freestream conicity on various point properties in the flow over a sphere—including the boundary layer thickness and tangential velocity gradient, which have never been examined before to any extent in the literature—is shown in figure 10. The qualitative trends exhibited by these properties from the influence of freestream conicity have intuitive physical interpretations. The 'y' component (see figure 3) of the freestream velocity immediately upstream of the shock (and not exactly on the axisymmetry axis) becomes more prominent with increasing freestream conicity. Near the axisymmetry axis, the shock is aligned almost parallel with the y-axis which allows this increasing 'y' velocity to transfer through the shock and hereby increasing the tangential velocity and tangential velocity gradient in the flow behind the shock in this region, as shown in figure 10 (c) for the tangential velocity gradient at the boundary layer edge on the axisymmetry axis. This increased tangential velocity gradient duly causes the sonic condition to be reached after a shorter distance and, consequently, shifts the sonic point closer to the axisymmetry axis as

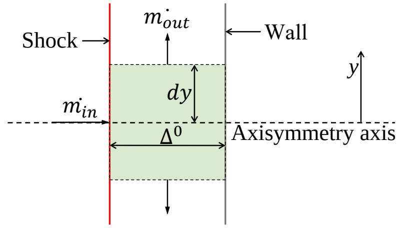

Figure 9: Inviscid flow over a sphere in the vicinity of the axisymmetry axis.

shown in figure 10 (b). Also, the increased tangential velocity increases the inertial force (over the viscous force) in the flow making the boundary layer thinner, as shown in figure 10 (d). Because the boundary layer edge pressure, density and temperature on the axisymmetry axis are essentially unchanged with freestream conicity, this thinner boundary layer directly increases the temperature gradient at the wall near the axisymmetry axis resulting in a larger heat flux as shown in figure 10 (e). Furthermore, as indicated in figure 10 (a), the increased tangential velocity forces the shock standoff distance near the axisymmetry axis to decrease, considering the control volume in figure 9, to maintain $\dot{m}_{in} = \dot{m}_{out}$ since both the flow density leaving the control volume and $\dot{m}_{in}$ are essentially uninfluenced by freestream conicity. This statement can be formulated mathematically as follows, assuming the tangential velocity is constant across the shock layer, an idea from Hornung (2019), and equal to $\left[(du/dx)^0\, dy\right]$,

$$\overline{\rho}^{out}_{\infty} \left[\left(\frac{du}{dx} \right)^0_{\infty} dy \right] 2\pi dy \Delta^0_{\infty} = \overline{\rho}^{out} \left[\left(\frac{du}{dx} \right)^0 dy \right] 2\pi dy \Delta^0 \tag{4.1}$$

where ρ^{out} is the average density leaving the control volume. The LHS corresponds to $\dot{m}_{out}$ in a uniform freestream while the RHS corresponds to that in a conical freestream. Assuming $\rho^{out} = \overline{\rho}^{out}_{\infty}$, one obtains

$$\frac{\left(\frac{du}{dx}\right)^0}{\left(\frac{du}{dx}\right)^0_{\infty}} = \frac{\Delta^0_{\infty}}{\Delta^0} \tag{4.2}$$

which can actually be obtained from equation 2.8 if one assumes $(R_s + \Delta^0)/(R_s + \Delta^0_{\infty}) \approx 1$, that is the change in shock standoff distance caused by freestream conicity is negligible compared with the distance between the shock and the center of the sphere (appropriate since the shock layer is generally thin in hypersonic flows); shown in figure 10 (c), this is a fine approximation as equation 4.2 agrees well with the other results, which also validates the simple model used in its derivation.

Examining the different results for the shock stand-off distance on the symmetry axis, figure 10 (a), one can see that the theoretical results match the numerical results well, with errors of less than ± 0.03 at $d = 4$. The influence of freestream conicity on the shock stand-off distance is shown to mostly have little sensitivity to the freestream condition; the PG results at different Mach and Reynolds numbers are essentially identical, differing by less than 0.03 for $d = 4$, consistent with the finding of Golovachov (1985). The EQ result is also very similar to the PG results, which is consistent with the finding of Golovachov (1985) and Shapiro (1975) who suggested that PG and EQ flows have the same influence from the freestream conicity. On the other hand, the NONEQ results do have a more noticeable difference from the other results. More precisely, the freestream conicity is shown to have a lesser influence on the

NONEQ conditions compared with the other conditions. This can be explained as follows. Because the freestream conicity causes the shock stand-off distance to decrease, the flow along the stagnation streamline becomes more frozen, which is obvious when examining the Damköhler number for O_2 dissociation (which is the main reaction occurring in the inviscid flow in the NONEQ condition) written as (following Candler (2018))

$$Da^0_{sk} = \frac{\Delta^0 k_{D,O_2} p_p}{\overline{u^0} T_p \mathcal{R}} \tag{4.3}$$

where $\overline{u^0}$ is the mean post-shock velocity on the stagnation streamline, $\mathcal{R}$ is the universal gas constant, T_p and p_p are the equilibrium post-shock total temperature and pressure, respectively, and k_{D,O_2} is the oxygen dissociation rate constant at T_p ($Da^0_{sk} = O(0)$ for the NONEQ condition); since the freestream condition immediately upstream of the shock on the stagnation streamline is unchanged, $\overline{u^0}$, T_p, p_p, and k_{D,O_2} are essentially uninfluenced by freestream conicity which means Da^0_{sk} decreases due to the smaller shock standoff distance (e.g. $(Da^0_{sk})^{d=4}/(Da^0_{sk})^{d=\infty} = \Delta^0_{d=4}/\Delta^0_\infty = 0.77$), leading to a more frozen flow along the stagnation streamline. However, such freezing tends to increase the shock stand-off distance as shown by Wen & Hornung (1995). Consequently, this results in the nonequilibrium flow having a resistance to the decrease in shock stand-off distance caused by the freestream conicity; such resistance is uniquely a nonequilibrium effect and is non-existent in PG and EQ flows.

Equation 2.4 from Hornung (2019) assumes the average density across the shock layer on the stagnation streamline outside of the boundary layer remains constant, which is true for perfect gas or equilibrium flows. For nonequilibrium flows, this average density does change with freestream conicity as shown in figure 11 which shows the density on the stagnation streamline between the shock and the boundary layer edge (defined as the wall-normal distance where the local total enthalpy is 99 % of the freestream total enthalpy). In this case, Hornung's equation should be given as,

$$\frac{\Delta^0}{\Delta^0_\infty} = \frac{\bar{\rho}^0_\infty}{\bar{\rho}^0} \frac{1}{1 + \frac{(R^0_c)_\infty}{L_1}} \tag{4.4}$$

where $\bar{\rho}^0$ and $\bar{\rho}^0_\infty$ are the average density across the shock layer on the stagnation streamline outside of the boundary layer in the nonuniform and uniform freestreams, respectively. Therefore, although thermodynamics was not explicitly considered in Hornung's derivations, the effect of nonequilibrium flow is allowed to enter through the average density across the shock. Figure 11 indicates that the average density across the shock in the $d = 4$ flow is about $4 - 5\%$ lower than that in the uniform flow which, according to equation 4.4, means the nonequilibrium value of Δ^0/Δ^0_∞ at $d = 4$ should be higher than the perfect or equilibrium gas value by the same amount; this is indeed observed in the results shown in figure 10 (a) when comparing the NONEQ results with the PG and EQ results from CFD.

To examine the importance of freestream conicity, the result in figure 10 (a) is compared with the experimental uncertainties for the shock stand-off distance as shown in table 2. The influence from the freestream conicity becomes comparable to the total uncertainty when $d \lessapprox 10$. If a unique freestream estimate for each individual shot is available, then the uncertainty from the test condition repeatability is eliminated and only the measurement uncertainty needs to be considered, in which case the influence from the freestream conicity becomes relevant when $d \lessapprox 20$. Therefore, because d as small as around 4 can realistically be encountered as discussed in section 1, experimental measurements of the shock stand-

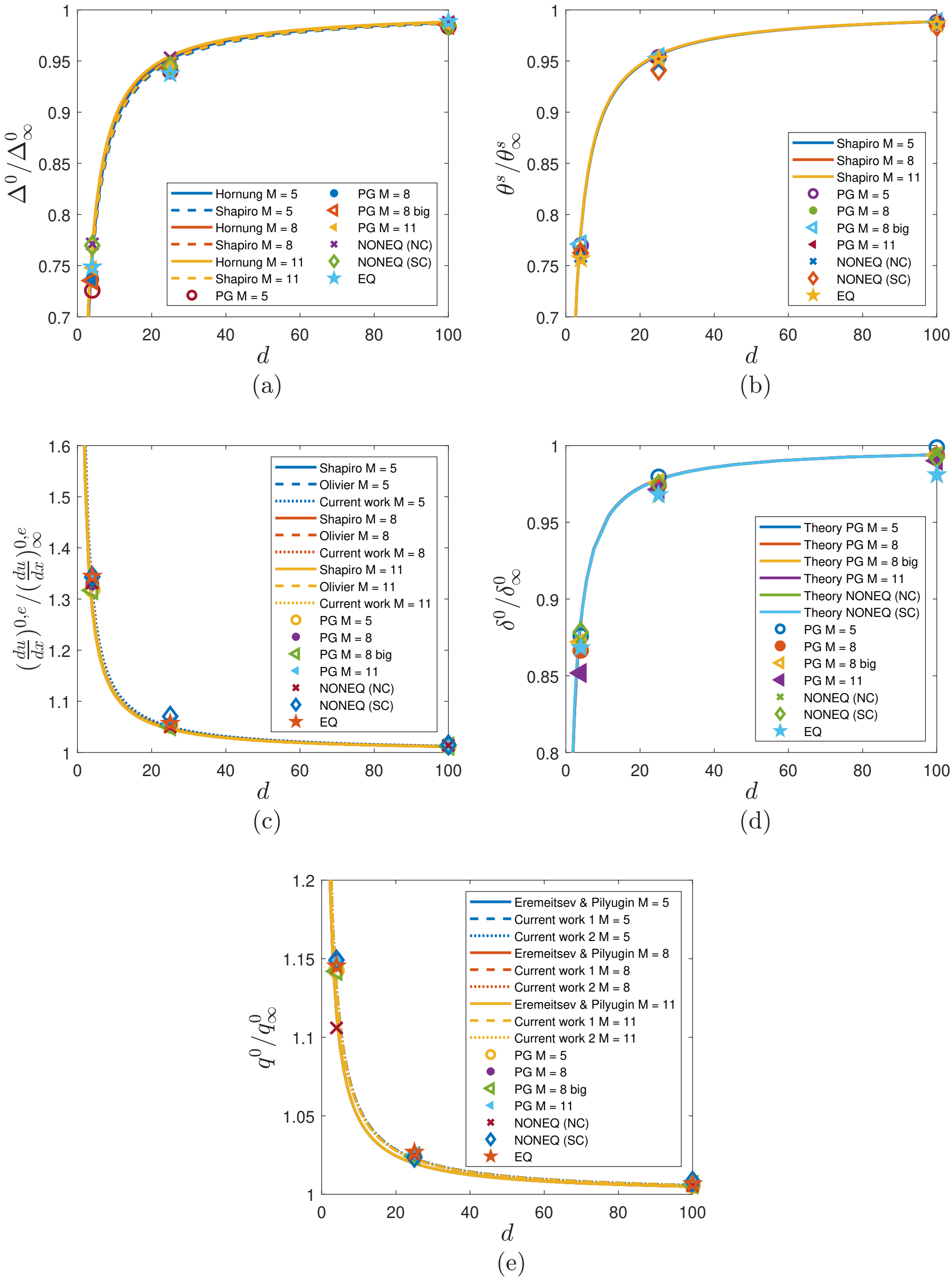

Figure 10: The influence of the degree of freestream conicity, measured by d, on the (a) shock standoff distance on the symmetry axis ('Hornung' and 'Shapiro' are from equations 2.4 and 2.1, respectively), (b) sonic point location ('Shapiro' is from equation 2.2), (c) tangential velocity gradient at the boundary layer edge on the stagnation streamline ('Shapiro', 'Olivier', and 'Current work' are from equations 2.10, 2.8, and 4.2, respectively), (d) boundary layer thickness at the stagnation point, and (e) stagnation point heat flux ('Eremeitsev & Pilyugin', 'Current work 1', and 'Current work 2' are from equations 2.6, 2.9, and 2.11, respectively).

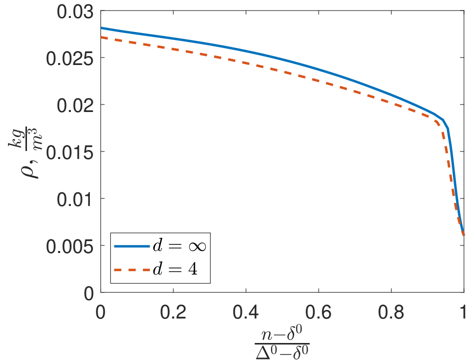

Figure 11: The density on the stagnation streamline between the shock and the boundary layer edge for Condition 5 (NONEQ) with a non-catalytic wall. Since 'n' is the normal distance from the wall and δ^0 is the boundary layer thickness at the stagnation point, the x-axis shows the normal distance from the boundary layer edge normalised with the shock-standoff distance.

off distances made in facilities with conical nozzles may be significantly influenced by the divergent freestream and, thus, this should be considered and checked before interpreting the experimental results. If corrections are required, they can be done easily using the analytical expressions that are shown in the current work to be very accurate (within the measurement uncertainty shown in table 2).

It is very interesting to observe that the two theoretical results (Shapiro (1975); Hornung (2019)), which were derived from different methods and have completely different expressions (equations 2.1 and 2.4), produce essentially the same curves in figure 10 (a). The Shapiro expression requires the calculation of the influence of freestream conicity on the sonic point location, θ^s/θ^s_∞, as a priori; an analytical expression for this is provided (equation 2.2) and its comparison with the numerical results is shown in figure 10 (b). One can see that the expression is very accurate, matching with the numerical results which are found at the boundary layer edge defined as the location where the local total enthalpy is 99 % of the freestream total enthalpy. All the results, including the NONEQ and EQ results, are essentially identical at a given d, which means that the results are not condition-dependent. The overall excellent prediction of θ^s/θ^s_∞ is a significant result as this value is also required as an important priori for the Shapiro transformation (Shapiro 1975), introduced in section 2.1, for the property distributions.

For the sonic point and tangential velocity gradient, shown in figures 10 (b) and (c), respectively, the fact that the NONEQ results are essentially indistinguishable from the other results may be surprising given that the NONEQ shock stand-off distance displays a resistance that may transfer to the tangential velocity gradient as shown in equations 2.8 and 4.2 which may, in turn, influence the sonic point location. However, equation 2.8 is for perfect gas and equilibrium flows; for nonequilibrium flows, the relationship should, instead, be derived from Olivier (1995) as

$$\left(\frac{du}{dx}\right)^{0,e} \propto \frac{R_s + \Delta^0}{\Delta^0}\frac{1}{\rho^{0,e}} \tag{4.5}$$

because the density at the boundary layer edge on the stagnation streamline, $\rho^{0,e}$, depends on the thermochemistry along the stagnation streamline which is influenced by freestream conicity, which is unlike in perfect gas and equilibrium flows where $\rho^{0,e}$ is uninfluenced in this way. In nonequilibrium flows, the freestream conicity makes the flow near the stagnation

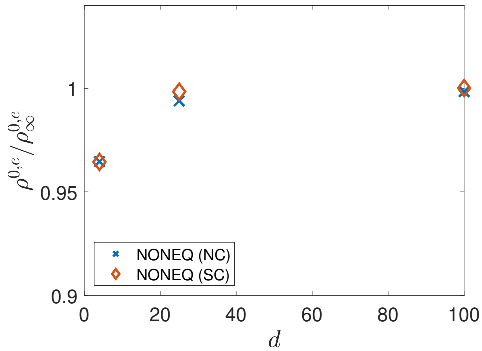

Figure 12: The influence of the degree of freestream conicity on the density at the boundary layer edge on the stagnation streamline.

streamline more frozen, which decreases the density (Anderson 2019); this is shown in figure 12 where the nonequilibrium effect reduces $\rho^{0,e}$ by about 4 % at $d = 4$ which is comparable to its effect on the shock stand-off distance where the NONEQ results at $d = 4$ are about 4 % greater than the other results, as shown in figure 10 (a). Consequently, the effect of the reduction in $\rho^{0,e}$ on $(du/dx)^{0,e}$ cancels out the effect of the resistance in shock stand-off distance resulting in $(du/dx)^{0,e}$ effectively having no special nonequilibrium effect as shown in figure 10 (c) where the analytical perfect or equilibrium gas results obtained using equation 2.8 (along with equation 2.4 to analytically predict the change in Δ^0) gives excellent agreement with all the numerical results. Likewise, retaining the density terms in equation 4.1, one obtains

$$\frac{\left(\frac{du}{dx}\right)^{0,e}}{\left(\frac{du}{dx}\right)^{0,e}_\infty} = \frac{\overline{\rho}^{out}_\infty}{\overline{\rho}^{out}} \frac{\Delta^0_\infty}{\Delta^0} \tag{4.6}$$

with allows nonequilibrium effects to enter through the density ratio. As shown in figure 11, nonequilibrium reduces the average density by about $4-5$% which is canceled out by its effect on the shock standoff distance resulting in the tangential velocity gradient ratio to be effectively uninfluenced by nonequilibrium according to equation 4.6. This cancellation can be expected from theory (conservation of mass) where the product $[\overline{\rho}^{out}\Delta^0]$ is known to be a constant for a given freestream and sphere size regardless of the thermochemistry involved (Wen & Hornung 1995).

Furthermore, due to the lack of nonequilibrium effects on the sonic point location and tangential velocity gradient, equation 2.10 from Shapiro (1975), which assumes a linear velocity distribution on the boundary layer edge between the axisymmetry axis and the sonic point, also predicts the tangential velocity gradient accurately as shown in figure 10 (c) (basically indistinguishable from Olivier's method). Shapiro mentioned that the error of his equation due to the aforementioned assumption is no larger than 5%; this is further confirmed in the current work by comparing with the CFD results. From CFD, the velocity distribution is essentially linear - with only a slight concave down curvature - as shown exemplarily for Condition 4 (PG $M = 11$) in figure 13. Shapiro's equation actually gives the ratio of the average tangential velocity gradient between the axisymmetry axis and the sonic point. Although the tangential velocity gradient at $\theta = 0$ is slightly higher than the average value due to the slight concave down curvature, this same trend is observed in both the uniform and nonuniform freestream simulations, as shown in figure 13, allowing the errors to essentially cancel out resulting in a good prediction of the ratio at $\theta = 0$.

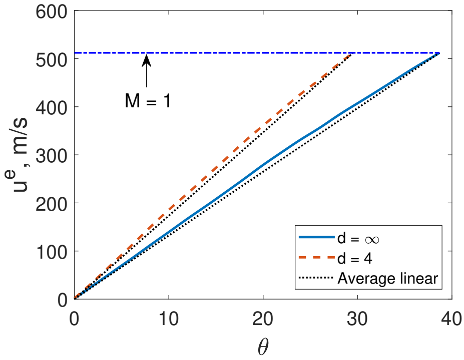

Figure 13: The boundary layer edge velocity, u^e, distribution between the axisymmetry axis and the sonic point for Condition 4 (PG $M = 11$).

The boundary layer thickness at the stagnation point—defined as the wall-normal distance where the local total enthalpy is 99 % of the freestream total enthalpy—is examined in figure 10 (d). One can see that the freestream conicity decreases the boundary layer thickness at the stagnation point, and the results are rather insensitive to the different flow conditions at any given d. Shown together with the Navier-Stokes solutions in this figure are the PG and NONEQ results from the numerical solutions of the self-similar boundary layer at the stagnation point of a sphere, which are denoted as 'Theory'. This theory (Anderson 2019) does not explicitly account for freestream conicity. However, as discussed earlier, freestream conicity influences the tangential velocity gradient at the stagnation point which can be varied in the aforementioned theory to possibly predict the influence of the freestream conicity on the boundary layer thickness at the stagnation point. Using the tangential velocity gradient at the stagnation point for a uniform freestream calculated analytically with Newtonian theory, and using equations 2.4 and 2.8 to calculate the change in tangential velocity gradient with freestream conicity, d, while all other boundary layer edge (stagnation point) properties remain unchanged for each condition (equilibrium stagnation conditions are used as the edge conditions in the NONEQ cases), the theoretical results are produced and excellent agreement with CFD is observed. This indicates, firstly, the freestream conicity decreases the boundary layer thickness solely due to the tangential velocity gradient, which increases due to the decreasing shock stand-off distance, and, secondly, the self-similarity of the boundary layer at the stagnation point is uninfluenced by freestream conicity. Furthermore, the results indicate essentially no dependence on the flow condition and gas type. No distinct nonequilibrium effects are observed which means that the changes to the edge condition caused by nonequilibrium as mentioned earlier do not significantly influence the boundary layer thickness.

The result for the stagnation point heat flux is shown in figure 10 (e) where the freestream conicity is found to increase the stagnation point heat flux which is expected given the nonuniformity decreases the shock stand-off distance which increases the tangential velocity gradient as discussed earlier in section 2.1. The theoretical results again match the numerical results well; the error is less than ±0.03 at $d = 4$. Also, the three theoretical results, which come from different expressions with different origins (equations 2.6, 2.9, and 2.11), are essentially identical. The results for the stagnation point heat flux, like with the shock stand-off distance, are mostly insensitive to the flow condition and gas type. The exception here is the NONEQ result using an NC wall which is a little lower than the other results as can be clearly seen when examining the $d = 4$ results. Interestingly, the NONEQ result using a SC wall does not exhibit this result. Consequently, it is found that the cause of the

NONEQ NC result differing from the other results is due to the nonequilibrium effect in the boundary layer. The thinning of the boundary layer at the stagnation point (which is almost frozen) with increasing conicity, discussed above, allows even less recombination to occur in the boundary layer as demonstrated in the Navier-Stokes solution of Condition 5 NC wall shown in figure 14; this same trend is also observed in the solutions of the NONEQ NC self-similar boundary layer. This phenomenon can also be shown through the gas-phase oxygen recombination Damköhler number (also called the recombination rate parameter) for the stagnation point boundary layer given as (Fay & Riddell 1958; Inger 1963)

$$Da_{BL}^{0} = \frac{k_{r,O_2} p_p^2}{(du/dx)^{0,e} T_p^2 \mathcal{R}^2} \tag{4.7}$$

where k_{r,O_2} is the oxygen recombination rate constant at T_p ($Da_{BL}^0 = \mathcal{O}(-4)$ for the NONEQ condition). Because the freestream condition immediately upstream of the shock on the stagnation streamline is unchanged, the only parameter in the above equation that changes due to freestream conicity is $(du/dx)^{0,e}$ which increases with increasing freestream conicity as mentioned earlier. Therefore, Da_{BL}^0 decreases with increasing freestream conicity due to the increasing $(du/dx)^{0,e}$ (e.g. $(Da_{BL}^0)^{d=4}/(Da_{BL}^0)^{d=\infty} = (du/dx)_{\infty}^{0,e}/(du/dx)_{d=4}^{0,e} = 0.75$), which is also shown earlier to decrease the boundary layer thickness, resulting in a more frozen boundary layer, and this is consistent with the CFD results. This phenomenon, consequently, results in less heat release in the boundary layer and a lower heat flux when the wall is noncatalytic (Fay & Riddell 1958).

On the other hand, if the wall is super-catalytic, the nonequilibrium in the boundary layer becomes irrelevant in terms of predicting the heat flux as shown by Fay & Riddell (1958). That is, the heat flux at a super-catalytic wall is essentially the same regardless of the behaviour of the chemical kinetics in the boundary layer. This is further demonstrated in figure 15 which shows the solutions from the nonequilibrium self-similar boundary layer with varying tangential velocity gradient while the other boundary layer edge conditions remain constant and equal to the equilibrium stagnation point condition of Condition 5. The results show that the heat flux scales perfectly with $\sqrt{(du/dx)^{0,e}}$ when the wall is super-catalytic, but not when the wall is non-catalytic due to the inhibiting of recombination by boundary layer thinning. Therefore, the NONEQ SC result in figure 10 (e) is not affected by the aforementioned phenomenon and, hence, agrees well with the other results. As a corollary, one can suggest that equation 2.7, which works very well for perfect gas and equilibrium flows, also works very well for nonequilibrium flows when the wall is super-catalytic, and this is consistent with the results of Fay & Riddell (1958).

To examine the importance of freestream conicity, the result in figure 10 (e) is compared with the experimental uncertainties for the surface heat flux as shown in table 2. The influence from the freestream conicity becomes comparable to the total uncertainty when $d \lessapprox 3$. In this case, given the context of the experimental uncertainty, the influence from the freestream divergence may generally be considered insignificant as it is within the experimental uncertainty even when the largest possible test model is used. However, if a unique freestream estimate for each individual shot is available, then the influence from the freestream conicity becomes relevant when $d \lessapprox 10$, and, thus, corrections to the experimental results may be necessary in certain cases which can easily be carried out using the analytical expressions given in the current work which are shown to be very accurate (within the measurement uncertainty shown in table 2).

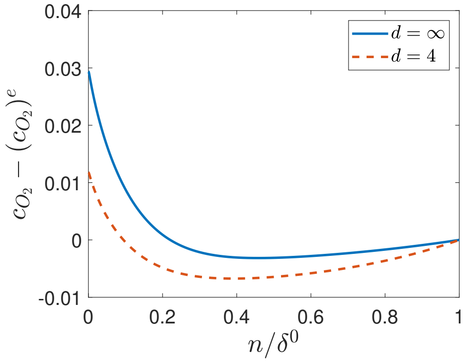

Figure 14: The O_2 mass fraction, c_{O_2}, distribution in the stagnation point boundary layer of Condition 5 (NONEQ) with a non-catalytic wall, where 'n' is the normal distance from the wall and superscript 'e' refers to the boundary layer edge.

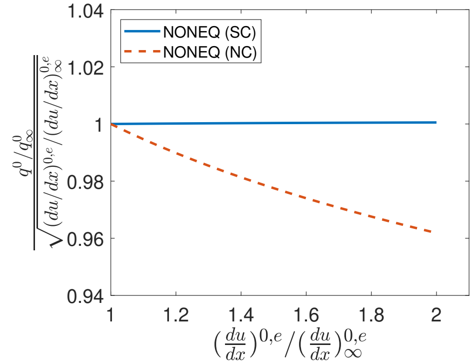

Figure 15: The solutions of the nonequilibrium self-similar stagnation point boundary layer for Condition 5 (NONEQ) with varying tangential velocity gradient.

4.2. *Distributions*

The influence of freestream conicity on various normalized distributions in the flow over a sphere is shown in figure 16. Although these normalized distributions are insensitive to the freestream condition in a uniform flow as discussed in section 3, they are all significantly influenced by the freestream conicity. From hereon in, all the NONEQ results refer to the NC wall case because the SC wall case produces essentially the same results and no special wall catalycity effects are observed, therefore, it is appropriately omitted for clarity. Looking at the normalized shock stand-off distance distribution in figure 16 (a), one can see that the freestream conicity causes the normalized shock stand-off distance to increase. In other words, the shock angle at any given θ increases with increasing freestream conicity as shown exemplarily in figure 17. This is an expected observation considering the divergent freestream expands in the y direction which effectively turns the shock in the anti-clockwise direction about the origin, as seen in expansion fan/shock wave interactions (Nel *et al.* 2015). The increase is more severe the larger the angle is away from the stagnation point. At $\theta = 90°$ and $d = 4$, the normalized shock stand-off distance is around two times larger than that in the corresponding uniform freestream. For reference, the absolute shock stand-off distance distribution is shown exemplarily in figure 18 (a) for Condition 4. One can see that the shock stand-off distance on the symmetry axis decreases with decreasing d, as expected from the previous section. Decreasing d also increases the gradient ($d\Delta/d\theta$) throughout, resulting in the shock stand-off distance in the nonuniform flow to be eventually greater than that in the uniform flow when θ becomes large. This is why the normalized distributions have the qualitative trend shown in figure 16 (a).

Comparing figure 16 (a) with the experimental uncertainty shown in table 2, one can see that measurements of the normalized shock stand-off distance should be corrected for the influence of freestream conicity when θ is close to 90° at $d \approx 25$ and when $\theta \gtrapprox 30°$ at $d \approx 4$. The Shapiro transformation (Shapiro 1975), discussed in section 2.1, is found to give a reasonable prediction when θ is not too large ($\theta \lessapprox 40$ at $d = 4$) as shown in figure 16 (a), consistent with the finding by Golovachov (1985), which may be used to correct for the freestream conicity. At large θ, the Shapiro transformation is found to overpredict the normalized shock stand-off distance, and, thus, numerical methods must be used to correct for the freestream conicity in this case. An alternative transformation may be proposed, as mentioned in section 2.1, in which all the results (nonuniform and uniform) are assumed to coalesce when the distribution is given in terms of $\theta + \omega$ (where ω is the flow divergence angle at θ, defined earlier in section 2.1) instead of θ. That is, it assumes that the normalized shock stand-off distance at some $\theta = \theta_1$ in a uniform flow is equal to that at $\theta = \theta_1 - \omega$ in a nonuniform flow. This transformation, denoted as "Current work" in figure 16 (a), is found to underpredict the normalized shock stand-off distance which, together with the Shapiro transformation, forms the bounds on the more accurate numerical results. Regarding the numerical results, although the PG results for different freestream conditions show very little difference, the results do show some sensitivity to the thermochemistry as the EQ, NONEQ, and PG results differ slightly from each other which can be seen when looking at the $d = 4$ results.

Looking at figure 16 (c), one can see that the freestream conicity causes the normalized surface pressure to decrease. As discussed by Lunev & Khramov (1970), this can simply be explained with the Newtonian theory: in a conical freestream, as θ increases the freestream flow angle, ω, increases as well which effectively makes the body surface more parallel with the freestream (figure 3), compared with the corresponding uniform freestream, and this causes the pressure distribution to decrease more rapidly in a conical freestream. The decrease is more severe the larger the angle away from the stagnation point. Because freestream conicity does not influence the pitot pressure (Golovachov 1985), the normalized and absolute distributions have the same qualitative shape. Comparing figure 16 (c) with the experimental uncertainty shown in table 2, one can see that measurements of the normalized surface pressure should be corrected for the influence of freestream conicity when $\theta \approx 90°$ at $d \approx 100$, $\theta \gtrapprox 40°$ at $d \approx 25$, and $\theta \gtrapprox 10°$ at $d \approx 4$. The Shapiro transformation and the expression of Lunev & Khramov (1970) (equation 2.13) give similar results, and both are found to work reasonably well when θ is not too large ($\theta \lessapprox 50°$ at $d = 4$), allowing analytical corrections for the freestream conicity. When θ is too large ($\theta \gtrapprox 60°$ at $d = 4$), not only are the analytical methods inaccurate, but also the influence from the freestream conicity becomes dependent on the flow condition and gas type, consistent with the work of Golovachov (1985).

Looking at the normalized heat flux distribution in figure 16 (b), one can see that the freestream conicity causes the normalized heat flux to decrease, which is qualitatively the same trend seen in the normalized surface pressure distribution. This is expected considering the work of Lees (1956) who showed that the normalized heat flux distribution around a sphere is closely related to its normalized surface pressure distribution. The absolute heat flux distribution is shown exemplarily in figure 18 (b), and one can see that the stagnation point heat flux increases with decreasing d, as expected from the previous section, while the gradient $dq/d\theta$ is decreased (made steeper) throughout, resulting in the normalized distributions having the qualitative trend shown in figure 16 (b). Comparing figure 16 (b)

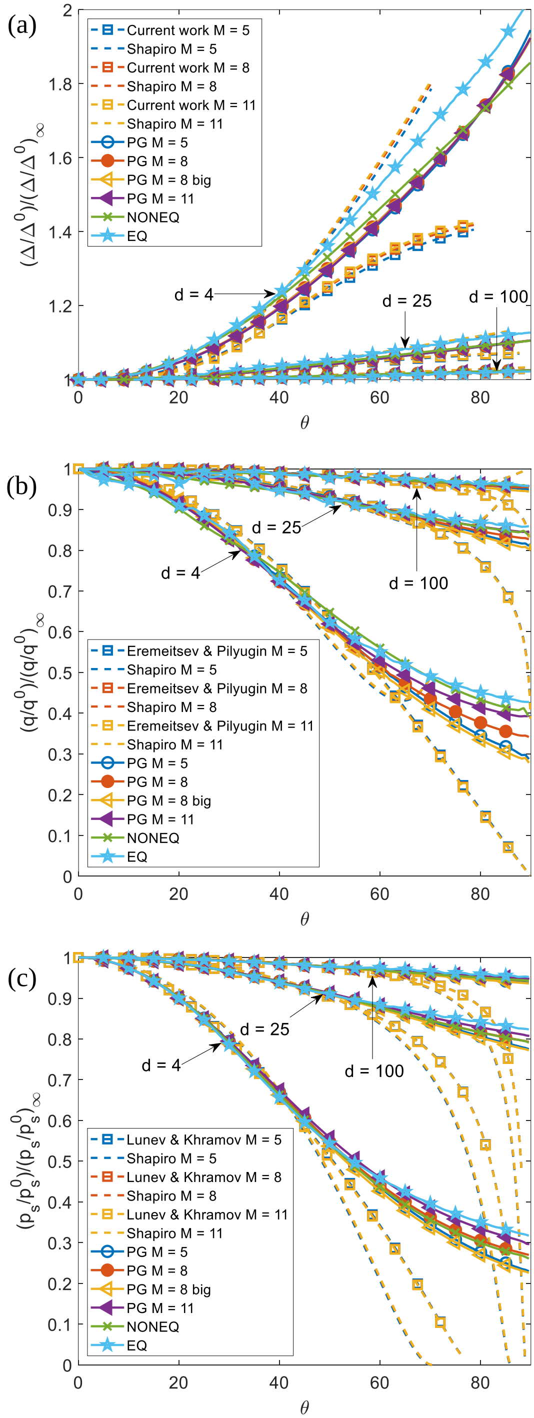

Figure 16: The normalized distributions of the (a) shock stand-off distance, (b) surface heat flux ('Eremeitsev & Pilyugin' is from equation 2.12), and (c) surface pressure ('Lunev & Khramov' is from equation 2.13). All 'Shapiro' refers to the Shapiro transformation (Shapiro 1975).

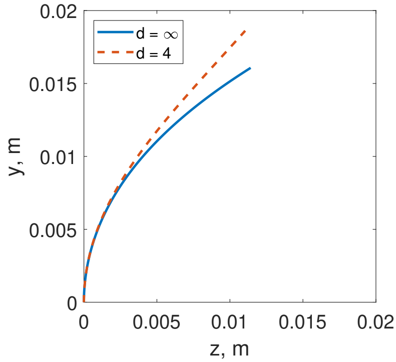

Figure 17: The shock locations for Condition 2 (PG $M = 8$). The curves are shifted on the x-axis such that they pass through the origin.

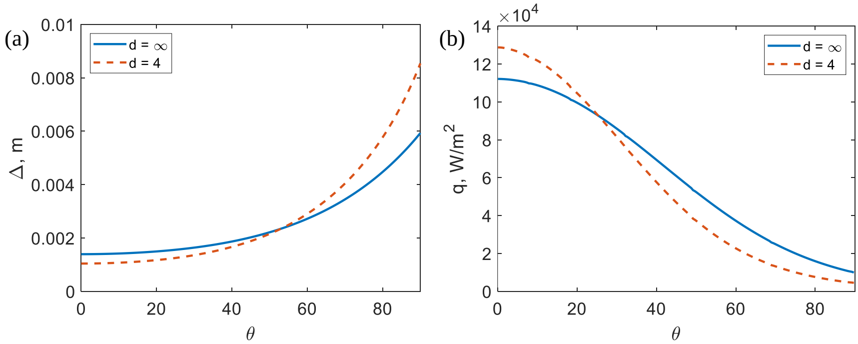

Figure 18: The absolute distributions of the (a) shock stand-off distance, and (b) surface heat flux for Condition 4 (PG M = 11).

with the experimental uncertainty shown in table 2, one can see that measurements of the normalized heat flux should be corrected for the influence of freestream conicity when $\theta \gtrsim 50°$ at $d \approx 25$ and when $\theta \gtrsim 20°$ at $d \approx 4$. The Shapiro transformation (Shapiro 1975) is found to work reasonably well when θ is not too large ($\theta \lesssim 50°$ at $d = 4$) as shown in figure 16 (a), consistent with the finding of Golovachov (1985), like with the normalized shock stand-off distance and pressure. The expression of Eremeitsev & Pilyugin (1984) (equation 2.12) gives results that are very similar to the Shapiro transformation in which good agreement with the numerical results is also attained when θ is not too large. Hence, in the case of θ not being too large, these two analytical methods are available for the correction of freestream conicity, while numerical methods are required otherwise. Also, when θ is not too large, the numerical results show that the influence from the freestream conicity is essentially independent of the freestream condition and thermochemistry; only when θ becomes large ($\theta \gtrsim 50°$ at $d \approx 4$) does the dependence on the flow condition and gas type show up which is similar to the normalized pressure and is consistent with the work of Golovachov (1985).

It should be mentioned that for the Shapiro transformation results shown in figure 16, the disagreement trend at large values of θ is not due to poor predictions of the corresponding uniform freestream distributions, required as a priori, obtained using the analytical expressions given by equations 2.15-2.17. This is because this disagreement exists even when the numerically obtained uniform freestream distributions are used, instead of the

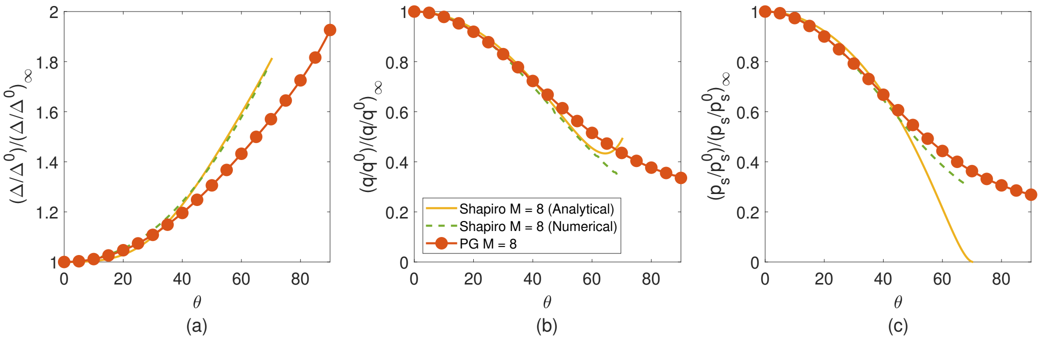

Figure 19: The normalized distributions of the (a) shock stand-off distance, (b) surface heat flux, and (c) surface pressure, for Condition 2 with $d = 4$ using Shapiro's transformation with uniform freestream distributions obtained analytically and numerically.

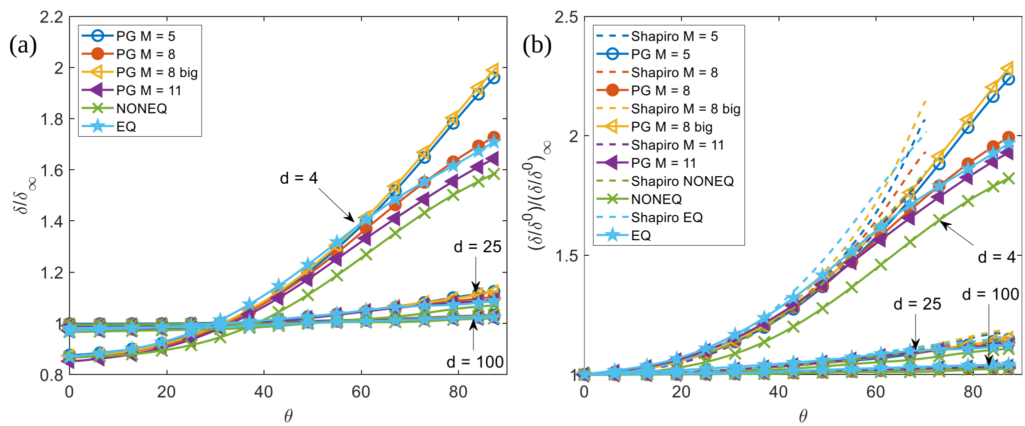

Figure 20: The influence of freestream conicity on the (a) boundary layer thickness at the stagnation point, (b) absolute boundary layer thickness distribution, and (c) normalized boundary layer thickness distribution.

analytical expressions, as the inputs for the Shapiro transformation. This is shown exemplarily in figure 19 for Condition 2 with $d = 4$. Therefore, the failure of the Shapiro transformation at large values of θ is inherent to the transformation itself rather than from the inputs. Nevertheless, for the surface pressure, significant quantitative improvements can be achieved at $\theta > 50°$ by using a more accurate input as shown in figure 19 (c), indicating equation 2.15 (from Newtonian theory) is inaccurate at larger values of θ; this makes sense because the shock lies far from the surface at large θ, hence, deviating from an ideal Newtonian flow (Anderson 2019). For the shock stand-off distance and heat flux distributions shown in figure 19 (a) and (b), respectively, no significant quantitative improvements are observed when using a more accurate input, indicating the analytical expressions are accurate enough.

For completeness, the boundary layer thickness—which has never been examined before in this context to any extent—is examined in figure 20. The freestream conicity decreases the boundary layer thickness at the stagnation point as discussed earlier. Downstream of the stagnation point, the freestream conicity causes the boundary layer thickness to grow rapidly as shown in figure 20 (a), and beyond about 30° the boundary layer thickness at any given θ becomes greater than that in the uniform freestream. This thickening of the

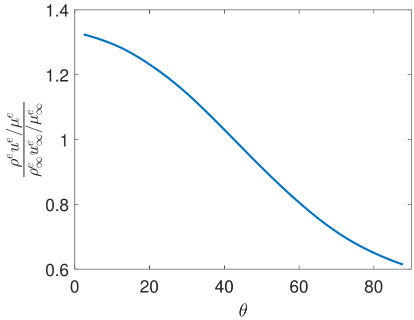

Figure 21: Ratio of the unit Reynolds number distribution using the boundary layer edge properties around a sphere between a conical freestream with $d = 4$ and a uniform freestream for Condition 1 (PG $M = 5$).

boundary layer caused by freestream conicity is consistent with the decrease in heat flux as shown in figure 16 (b). This is also consistent with the unit Reynolds number distribution as shown in figure 21; near the stagnation point, the inertial force relative to the viscous force is greater in a conical freestream due to the higher boundary layer edge velocity which results in a thinner boundary layer, while further away from the stagnation point the inertial force becomes relatively smaller in a conical freestream due to the lower boundary layer edge density resulting in a thicker boundary layer.

Regarding the normalized distribution, it is of interest to test if the Shapiro transformation also works with the boundary layer thickness. The result is shown in figure 20 (b) where the Shapiro transformation is applied to predict the distributions for $d = 4$, 25, and 100 using the normalized distributions for the uniform freestream computed from CFD. One can see that, similar to the normalized distributions of the other properties shown above in figure 16, good agreement is observed for most cases when θ is not too large (e.g. $\theta \lessapprox 50$ at $d = 4$). The exception is the NONEQ result which the Shapiro transformation does not work for, even at small values of θ. The results in figure 20 indicate that freestream conicity has a quantitatively different (lesser) influence on nonequilibrium flow where the differentiation with the other conditions is noticeable even at small values of θ; among the other conditions, the differentiation only becomes noticeable at large values of θ. This demonstrates another special nonequilibrium effect, non-existent in frozen and equilibrium flows, that is mild and is like the resistance shown by Δ^0 and by q^0 when the wall is non-catalytic as demonstrated above in section 4.1.

4.3. *Boundary Layer Transition*

Another aspect of the flow around a sphere worth examining is the boundary layer transition, which is observed experimentally. Despite substantial recent work on this topic, a theoretical understanding of the boundary layer transition on a blunt-body remains elusive (Paredes *et al.* 2017, 2018; Hein *et al.* 2019; Schilden *et al.* 2020; Di Giovanni & Stemmer 2018). The boundary-layer flow over a blunt body does not support the growth of modal instability waves, and this problem has been termed the "blunt-body paradox". Roughness-induced transient growth has been considered a possible cause; however, transient growth analysis for purely stationary disturbances in weakly nonparallel boundary layers and direct numerical simulations of the flow behind a roughness patch on a spherical forebody only found moderate energy amplification (Paredes *et al.* 2017, 2018; Hein *et al.* 2019). Due to the lack of theoretical foundations in this problem, the relevant research relies heavily on

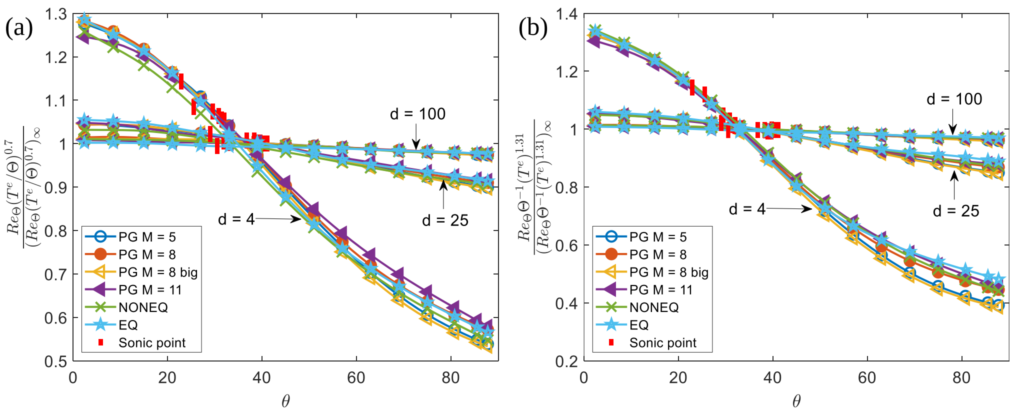

Figure 22: The influence of freestream conicity on the distribution of the LHS of equations (a) 4.8 and (b) 4.9, assuming k and T^w are constants.

experimentation which can, consequently, involve the use of conical nozzles (Lin *et al.* 1977).

Currently, the best way to predict the aforementioned transition is using semi-empirical correlations with inputs obtained via laminar CFD simulations. From experimental data, which show that transition always occurs in the subsonic region (upstream of the sonic point θ^s), the following correlation is given for a sphere (Paredes *et al.* 2017)

$$Re_\Theta \left(\frac{k}{\Theta}\frac{T^e}{T^w}\right)^{0.7} \begin{matrix} \geqslant \\ = \end{matrix} \begin{cases} 255 \text{ at } \theta^s : & \text{transition onset} \\ 215 : & \text{onset location} \end{cases} \tag{4.8}$$

where Θ is the boundary layer momentum thickness, k is the peak-to-valley roughness height, T^w is the wall temperature, T^e is the boundary layer edge temperature, and Re_Θ is the Reynolds number based on the momentum thickness and flow conditions at the boundary layer edge, $\rho^e u^e \Theta/\mu^e$. The correlation shows that the left-hand-side (LHS) of equation 4.8 has to exceed a value of 255 at the sonic point for transition to occur at all, and transition occurs at a point where the LHS of equation 4.8 equals 215. To study, for the first time, how freestream conicity affects the transition location in the flow over a sphere, the influence of freestream conicity on the LHS of equation 4.8 is shown in figure 22 (a), considering that k and T^w are uninfluenced. Examining this figure, one can see that the freestream conicity increases the value of the LHS in the subsonic region, which means that the transition location in the conical freestream, if transition were to occur, would occur closer to the stagnation point than in the uniform freestream. An alternative (and more recent) correlation to predict the onset location is given by Paredes *et al.* (2018)

$$Re_\Theta \left(\frac{k}{\Theta}\right)\left(\frac{T^e}{T^w}\right)^{1.31} = 455 \tag{4.9}$$

and the influence of freestream conicity on the LHS of this equation is shown in figure 22 (b); the same trend is observed. Also, both results in figure 22 show very little dependence on the flow condition and gas state. Equations 4.8 and 4.9 were derived for perfect gas flows, and, thus, their validity in reactive flows is unknown. Nevertheless, they are still applied to the nonequilibrium and equilibrium results in the current work due to the lack of any alternatives.

To understand the trend found in figure 22, it is of interest to examine the trends of the flow properties making up the LHS of equations 4.8 and 4.9; this is shown in figure 23. One can see that the increase in the value of the LHS in the subsonic region by freestream conicity is mainly due to the increase in the boundary layer edge tangential velocity, as shown in figure 23 (d), caused by the freestream conicity which is shown in section 4.1 to increase the tangential velocity gradient. With increasing freestream conicity, this increase in the edge velocity, together with the decrease in the edge viscosity shown in figure 23 (b), overcomes the contributions to decrease the LHS caused by the decrease in the edge density and temperature, shown in figure 23 (c) and (a), respectively, and the decrease in the momentum thickness in the subsonic region, shown in figure 23 (e). Downstream of the sonic point, the influence of the edge density and temperature wins over and the LHS is shown to decrease with increasing freestream conicity. However, what happens upstream of the sonic point is more important because current experimental data indicates that transition only occurs in the subsonic region.

Regarding the edge temperature (and, consequently, the viscosity) shown in figure 23, an exception to the mainstream trend can be observed in the NONEQ result where the freestream conicity is shown to cause an increase in the value in the subsonic region; this is the same phenomenon mentioned in section 4.1 where the freestream conicity is found to make the flow near the stagnation streamline more frozen, which increases the translational temperature because less energy is transferred to the vibrational and chemical modes. This phenomenon is also evident in the edge density results, with the NONEQ flow having its edge density in the subsonic region decreased more by the freestream conicity compared with the other conditions, as mentioned earlier in section 4.1.

In addition to examining the distribution of the values of the LHS of equation 4.8 in the subsonic region, it is also of interest to examine the value of the LHS of equation 4.8 at the sonic point because the LHS has to exceed a certain value at this location for transition to occur. The result is shown in figure 24 (a). One can see that the LHS at the sonic point decreases very slightly, $\approx 5 - 8\%$ at $d = 4$, with increasing freestream conicity for all the conditions. This is because, although freestream conicity increases the LHS at any given θ in the subsonic region, freestream conicity also shifts the location of θ^s closer to the stagnation point where the LHS has a lower value as shown exemplarily in figure 24 (b) for Condition 1. Ultimately, the shift of θ^s to a location with a lower value of the LHS slightly overcomes the overall increase of the LHS in the subsonic region, resulting in a slight decrease of the LHS at θ^s. Because this decrease is only very slight, it can be suggested that the freestream conicity will not influence whether transition occurs. Therefore, if transition occurs in a uniform freestream, it would also occur in a conical freestream, albeit with the transition point shifted upstream closer to the stagnation point as mentioned earlier in this section. This result shows no significant dependency on the flow condition and gas type.

Finally, to provide some idea of how much the transition point gets shifted upstream due to freestream conicity, figure 25 is produced. To systematize the comparison, k for each condition is selected such that the LHS of equations 4.8 and 4.9 is equal to 280 and 500, respectively, at the sonic point in the uniform freestream case; this value of k remains constant for the same condition at different d. The results show that the transition point can get shifted upstream by as much as $15 - 20\%$ and $20 - 25\%$ for the different conditions at $d = 4$ using equations 4.8 and 4.9, respectively, and demonstrate no significant dependency to the flow condition and gas type. Such a shift is significant, and it should be accounted for when interpreting the experimental results if a conical nozzle is used along with a significantly large spherical test model. Note that the results presented in figure 25 (and figure 24 (a)) are only given at discrete points because their calculation involves significant inputs from CFD which can only be obtained for a few values of d ($d = 4, 25, 100$). As indicated in equations

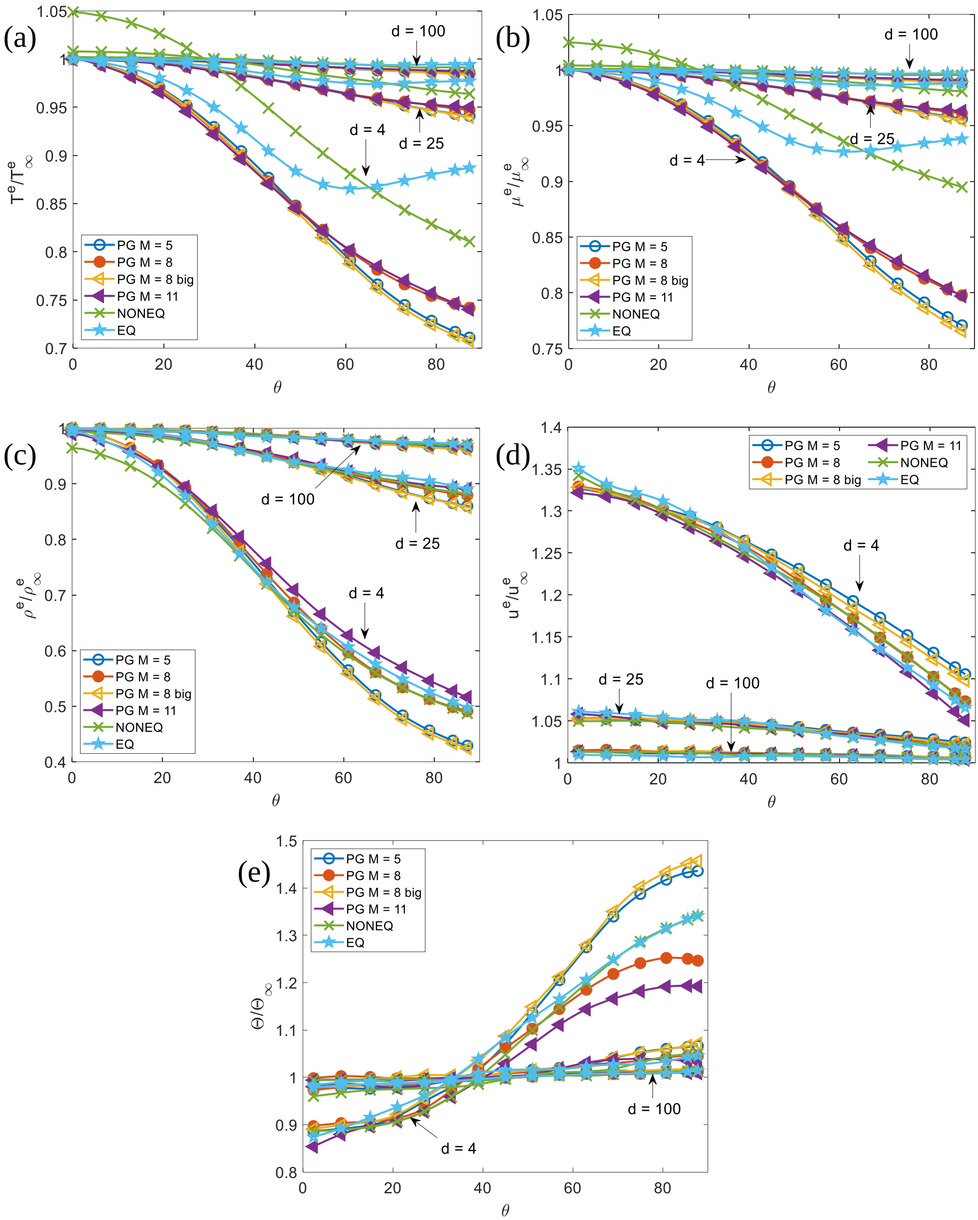

Figure 23: The influence of freestream conicity on the distribution of the (a) edge temperature, (b) edge viscosity (calculated using Sutherland's formula), (c) edge density, (d) edge tangential velocity, and (e) momentum thickness.

4.8 and 4.9, parameters such as the boundary layer momentum thickness, edge velocity, edge density, and edge temperature in both uniform and nonuniform freestreams are required, and these have to be attained using CFD. Consequently, the influence of freestream conicity on transition, unlike some of the other properties analyzed earlier, cannot be predicted purely analytically.

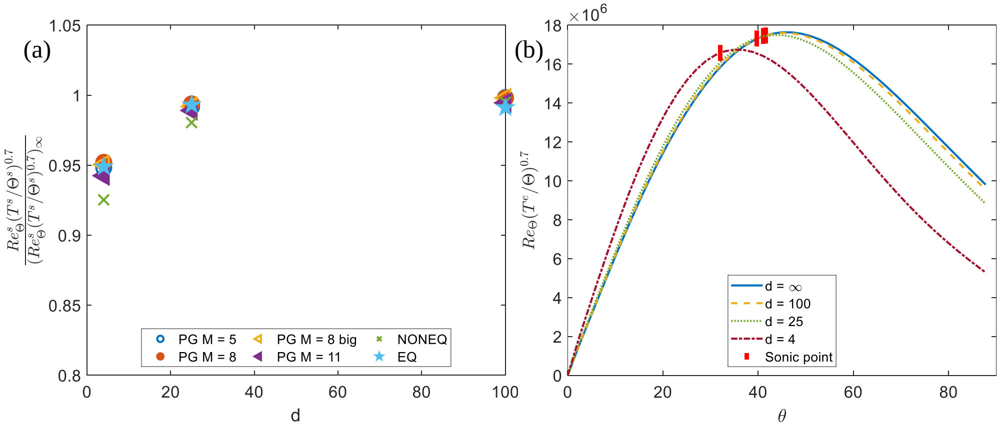

Figure 24: The (a) influence of freestream conicity on the value of the LHS of equation 4.8 at the sonic point, and (b) absolute distribution of the LHS of equation 4.8, without k and T^w which are constants, for Condition 1 (PG M = 5).

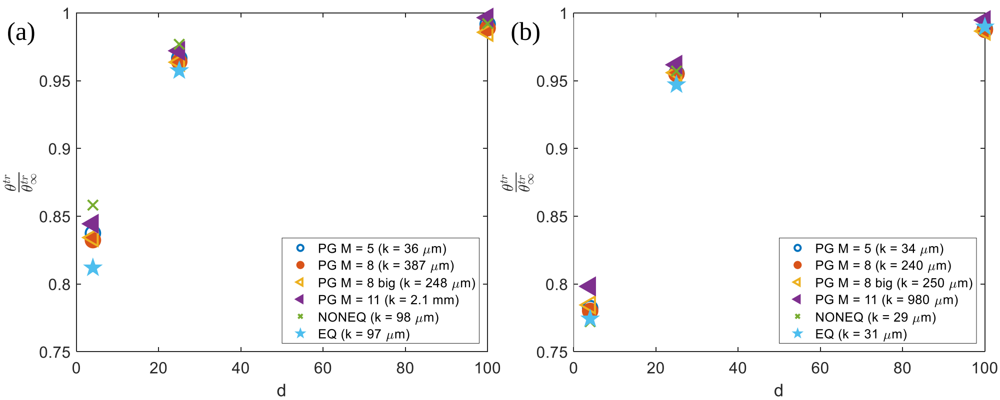

Figure 25: The influence of freestream conicity on the transition onset point, θ^{tr}, using equations (a) 4.8 and (b) 4.9. The wall temperature T^w is 295 K in all the cases.

4.4. *Flowfield*

For completeness, it is of interest to examine the entire flowfield. The results are exemplarily shown in 26 for Condition 2 (PG $M = 8$), and the same trends are observed in the other conditions. As expected from section 4.1, the shock standoff distance on the axisymmetry axis is clearly smaller in the conical freestream (bottom half) than in the uniform freestream (top half). Also, as shown in figure 26 (a), freestream conicity makes the entire sonic line move towards the axisymmetry axis, which is consistent with the sonic point results presented in section 4.1. Looking at figures 26 (e) and (f), one can see that the velocity in the z-direction does not change much with freestream conicity but the velocity in the y-direction does. Although the conical freestream expands in both directions, the shock is mostly aligned closer with the y-axis than the z-axis which allows more of the y component of the freestream velocity to transfer through the shock resulting in this observation. Examining figures 26 (b), (c) and (d), freestream conicity does not influence the pressure, temperature, and density near

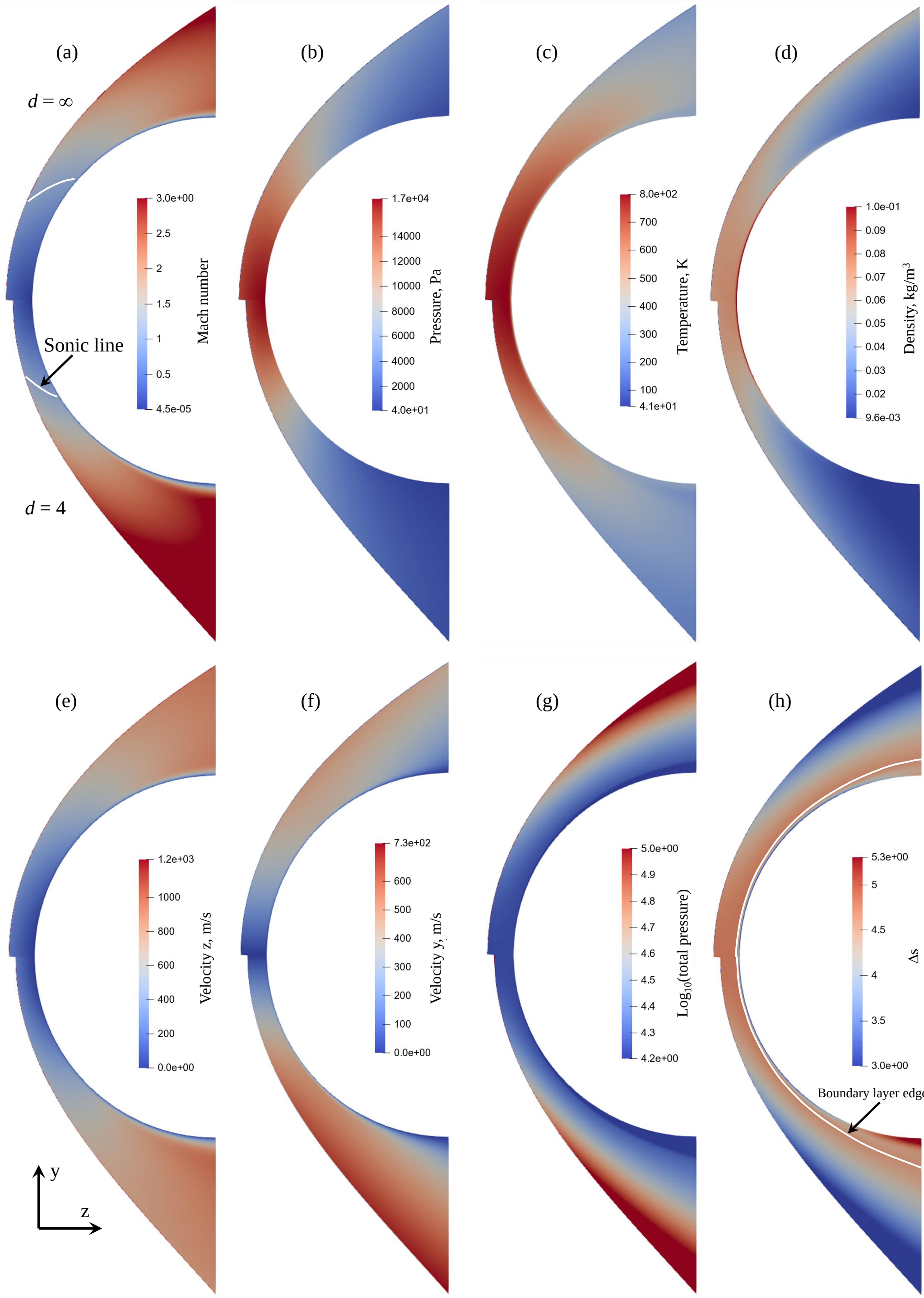

Figure 26: The Condition 2 (PG $M = 8$) flowfield (a) Mach number, (b) pressure, (c) temperature, (d) density, (e) velocity z, (f) velocity y, (g) total pressure, and (h) entropy $\left(\Delta s = \frac{\gamma}{\gamma - 1} \ln \frac{T}{T_\infty} - \ln \frac{p}{p_\infty}\right)$. The top half corresponds to a uniform freestream while the bottom half corresponds to $d = 4$.

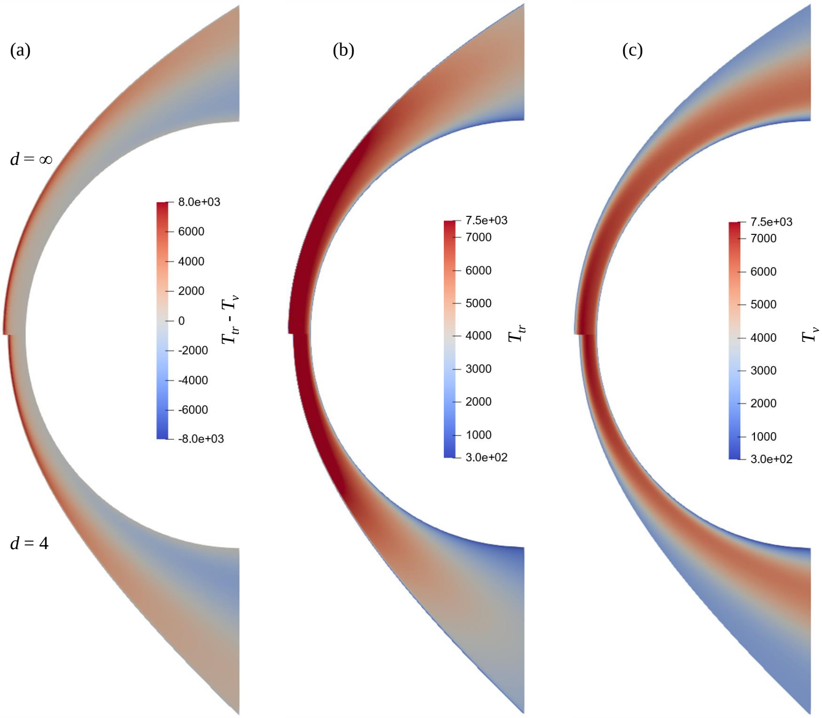

Figure 27: The Condition 5 (NONEQ) NC wall flowfield of the (a) difference between the translational-rotational temperature, T_{tr}, and vibrational temperature, T_v, (b) translational-rotational temperature, and (c) vibrational temperature.

the stagnation region but does decrease these parameters elsewhere, which is consistent with the corresponding distributions along the boundary layer edge as presented earlier in section 4, due to the expansion in the freestream. Finally, examining figures 26 (g) and (h), which are both indicative of the entropy variations in the flowfield, one can see that freestream conicity does not significantly influence the entropy distribution in the flowfield; in both the uniform and nonuniform freestream cases, the entropy at the boundary layer edge is approximately constant and equal to the entropy around the stagnation region, as expected in the flow over a sphere (Anderson 2019), and an entropy layer forms from the shock wave at $\theta \gtrapprox 40°$.

Further analysis is undertaken for the nonequilibrium condition to examine how freesteam conicity changes the thermochemical nonequilibrium behaviour in the flowfield. Thermal nonequilibrium is examined in figure 27 by looking at the difference between the translational-rotational temperature and vibrational temperature; the NC wall results are shown exemplarily, and the same is observed for the SC wall. The flow near the shock front has strong thermal nonequilibrium with T_{tr} being significantly greater than T_v while the flow in the boundary layer near the wall is essentially in thermal equilibrium, and no significant differences are observed between the uniform and conical freestream cases concerning these observations. On the other hand, the thermal nonequilibrium seen in the inviscid flow near the boundary layer edge at $\theta \gtrapprox 30°$, where T_v is significantly greater than T_{tr}, does exhibit a difference between the two freestream cases: the conical freestream produces stronger thermal nonequilibrium here. This is expected considering the flow expanding around the sphere from the stagnation region is further assisted by the expansion in the conical freestream resulting in a more rapid expansion due to freestream conicity leading to a stronger thermal nonequilibrium of this kind ($T_v > T_{tr}$). This is also consistent with the results shown above

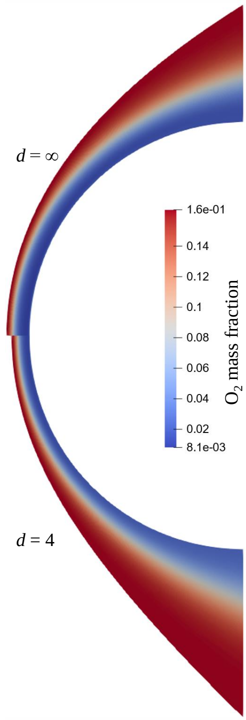

Figure 28: The Condition 5 (NONEQ) NC wall O_2 mass fraction, c_{O_2}, flowfield.

in this section where freestream conicity is found to increase the velocity and decrease the pressure, temperature (translational-rotational), and density in the flow over a sphere outside of the stagnation region. Consider the vibrational Damköhler number of the inviscid flow travelling around the boundary layer edge of the sphere (following from Passiatore *et al.* (2022)),

$$Da_v^e = \frac{R_s/u^e}{\tau_v} \tag{4.10}$$

where τ_v is the vibrational relaxation time ($Da_v^e = \mathcal{O}(0)$ for the current condition). The decrease in pressure and temperature by freestream conicity increases τ_v (Millikan & White 1963) which, together with the increase in u^e, decreases Da_v^e making the flow more vibrationally frozen (e.g. $(Da_v^e)^{d=4}/(Da_v^e)^{d=\infty} = 0.4$ using conditions at the boundary layer edge at $\theta = 45°$). Looking at figures 27 (b) and (c), the translational-rotational temperature is lower in the conical freestream case while the vibrational temperature remains basically the same between the two cases resulting in the larger thermal nonequilibrium seen in the conical freestream case.

To examine the finite-rate chemistry, which is dominated by the oxygen dissociation/recombination reaction in this condition, figure 28 is made which shows the O_2 mass fraction flowfield. Examining the difference between the uniform freestream and conical freestream results, the O_2 mass fraction distribution remains largely the same near the shock front while some differences can be observed in the inviscid region near the boundary layer edge, like with the thermal nonequilibrium. This can be seen more clearly in figure 29 (a) which shows the O_2 mass fraction along $\theta = 0°, 30°, 60°$ rays in the inviscid flow; the results in this figure are for an NC wall, and the same is observed for a SC wall. One can see that the O_2 mass fraction is always higher in the conical freestream, indicating inhibition of

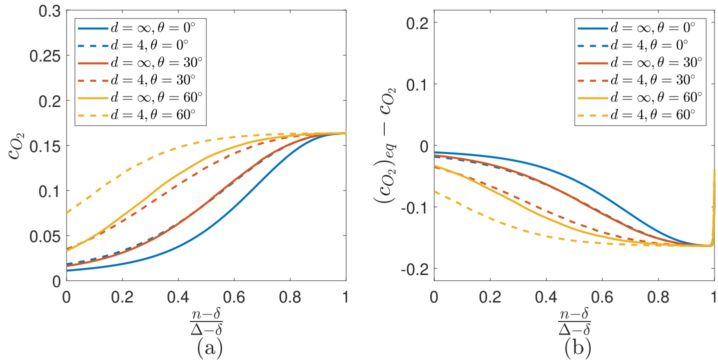

Figure 29: The (a) O_2 mass fraction, c_{O_2}, and (b) difference between the equilibrium O_2 mass fraction (at the local translational-rotational temperature and pressure), $(c_{O_2})_{eq}$, and the actual O_2 mass fraction in the inviscid flow along rays of $\theta = 0°, 30°, 60°$ for Condition 5 with NC wall. The x-axis is normalized to give the distribution between the shock front and boundary layer edge.

dissociation and the presence of larger chemical nonequilibrium. This is confirmed when examining figure 29 (b) which shows the difference between the equilibrium O_2 mass fraction (calculated using Cantera (Goodwin *et al.* 2023) at the local translational-rotational temperature and pressure) and the actual O_2 mass fraction in the inviscid flow. In this region the actual O_2 mass fraction is always in excess (dissociating nonequilibrium with $[(c_{O_2})_{eq} - c_{O_2}] < 0$), and one can see that freestream conicity generally increases the degree of this kind of chemical nonequilibrium here because the conical freestream results (dashed lines) are always lower than the uniform freestream results (solid lines) at all three θ values. The result for $\theta = 0°$ was already presented in section 4.1; for this case, the observation is caused by the smaller shock standoff distance as explained earlier. For the $\theta = 30°, 60°$ cases, the larger chemical nonequilibrium observed in the conical freestream is due to the same reason explained above for the larger thermal nonequilibrium: the expanding freestream assists the expansion of the flow around the sphere from the stagnation region resulting in a more rapid expansion which creates a larger nonequilibrium. Examining the O_2 dissociation Damköhler number which, for the current discussion, can be written as (following from Candler (2018))

$$Da_c^e = \frac{R_s \rho^e k_{D,O_2}}{u^e \mathcal{M}_{O_2}} \tag{4.11}$$

where $\mathcal{M}_{O_2}$ is the O_2 molar mass, and k_{D,O_2} is the O_2 dissociation rate constant which increases exponentially with temperature ($Da_c^e = O(-1)$ for the current condition). For the inviscid gas flowing around the sphere, the freestream conicity causes the velocity to increase, and the density and temperature to decrease, which all contribute to decrease the Da_c^e and make the flow more frozen (e.g. $(Da_c^e)^{d=4}/(Da_c^e)^{d=\infty} = 0.4$ using conditions at the boundary layer edge at $\theta = 45°$).

Finally, details of the gas-phase reaction in the boundary layer are important for the NC wall (unlike the SC wall) due to its influence on the wall heat flux as mentioned earlier (Fay & Riddell 1958). Therefore, to examine this more closely, figure 30 is made which shows the O_2 mass fraction along $\theta = 0°, 30°, 60°$ rays in the boundary layer with an NC wall. One can see that, in both the conical and uniform freestreams, the mass fraction does not change much through the boundary layer, especially when θ is not large, with only minor recombination occurring near the wall, indicating the boundary layer is basically frozen. Larger variation of the O_2 mass fraction is seen through the boundary layer at $\theta = 60$, particularly in the

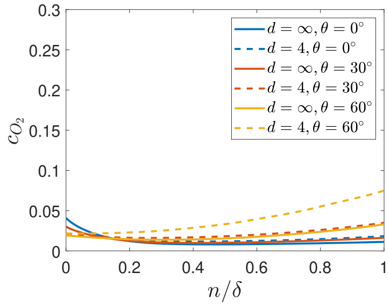

Figure 30: The O_2 mass fraction in the boundary layer along rays of $\theta = 0°, 30°, 60°$ for Condition 5 with NC wall. The x-axis is normalized to give the distribution between the wall and boundary layer edge.

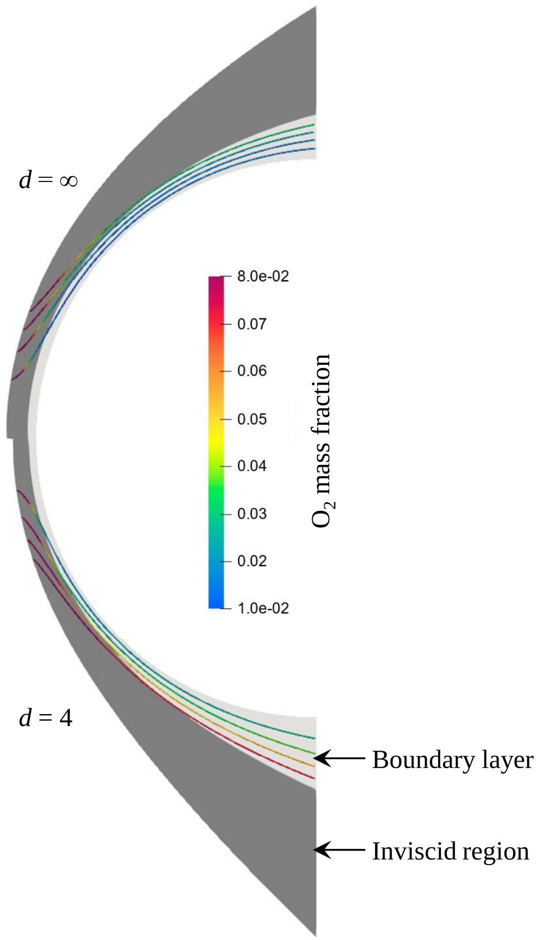

Figure 31: The Condition 5 (NONEQ) NC wall O_2 mass fraction streamlines overlaid on the inviscid and boundary layer flow domains represented by the dark gray and light gray contours in the background, respectively. The four streamlines pass through $\theta = 60$ at $n/\delta = 0.25, 0.5, 0.75, 1.0$.

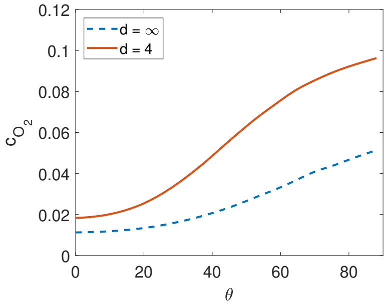

Figure 32: The Condition 5 (NONEQ) NC wall O_2 mass fraction along the boundary layer edge.

conical freestream, where the O_2 mass fraction is higher near the boundary layer edge and decreases with decreasing distance from the wall, but this is not due to chemical reactions happening in the boundary layer. This is due to the growing thickness of the boundary layer which swallows the inviscid flow with radially varying O_2 mass fraction, as seen in figures 28 and 29 (a) (similar to the entropy layer swallowing phenomenon (Anderson 2019)). In other words, at $\theta = 60$, the flow near the wall in the boundary layer originates from the inviscid region with $\theta \approx 0$ while the flow in the boundary layer near the boundary layer edge originates from the inviscid region with $\theta \gg 0$, resulting in the aforementioned O_2 mass fraction distribution through the boundary layer since the chemistry is essentially frozen in the boundary layer. This description is seen more clearly in figure 31 which shows four streamlines that pass through $\theta = 60$ at $n/\delta = 0.25, 0.5, 0.75, 1.0$. One can see that the mass fraction along the streamlines essentially freezes after entering the boundary layer. Because different streamlines enter the boundary layer with different mass fractions, an obvious mass fraction distribution forms through the boundary layer at larger values of θ despite the flow being basically frozen in the boundary layer. This distribution is, therefore, related to the O_2 mass fraction distribution along the boundary layer edge, which is shown in figure 32. Freestream conicity, in addition to reducing the dissociation in the inviscid flow as it expands around the sphere, also increases the rate of growth of the boundary layer, as mentioned earlier in section 4.2, making it swallow more of the inviscid flow; these factors combine to result in the O_2 mass fraction distribution along the boundary layer edge being higher and having a larger variation in the conical freestream, as shown in figure 32. This larger mass fraction variation along the boundary layer edge is directly responsible for the corresponding larger mass fraction variation through the boundary layer in the conical freestream seen in figure 30.

5. Conclusions

The influence of freestream conicity on the various aspects of the flow over a spherical test model, such as the shock wave, pressure, heat flux, and boundary layer, is examined using both analytical and numerical methods. For the analytical method, an easy-to-use closed-form analytical model is compiled which predicts the influence of freestream conicity without the need for any input from numerical computations. For the numerical method, the ‘Eilmer’ Navier-Stokes solver is used to perform 2D axisymmetric simulations of the flow around a sphere in freestreams with different degrees of conicity. Six different freestream conditions with different Mach numbers, Reynolds numbers, and thermochemistry are tested at four different degrees of conicity (d = ∞, 100, 25, 4) corresponding to that which can realistically be encountered in experiments. The numerical work included thermochemical nonequilibrium simulations; this is unlike the previous studies that examine the influence of freestream conicity, which only consider perfect gas or equilibrium flows. Also unlike the previous works, the current work is fully related to practical experimental scenarios by considering the realistic range of 'd' and by considering the uncertainties (measurement uncertainties and shot-to-shot variations) of hypersonic experiments. Furthermore, the influence of freestream conicity on the tangential velocity gradient, boundary layer thickness, and boundary layer transition is considered for the first time in this paper. In addition to answering the important question of just how much the freestream conicity influences the experiments, the underlying physics involved is thoroughly explained as well, which is not discussed in many of the earlier works which mostly only look to predict and quantify the influence of freestream conicity without really attempting to provide a physical explanation for the observations.

The shock stand-off distance on the symmetry axis, Δ^0, is shown to decrease with increasing freestream conicity. The decrease in Δ^0 increases the tangential velocity gradient at the stagnation point which increases the stagnation point heat flux, q^0, and decreases the stagnation point boundary layer thickness, δ^0. Excellent agreement between the analytical and numerical results is observed for Δ^0/Δ^0_∞ and q^0/q^0_∞, with errors of less than ± 0.03 at $d = 4$. This same level of agreement is observed between self-similar boundary layer theory and numerical results for δ^0/δ^0_∞. Considering the experimental uncertainties, measurements of Δ^0 and q^0 made in facilities with conical nozzles may be significantly influenced by the divergent freestream and, thus, this should be considered and checked before interpreting the experimental results. The influence of d on these properties is also mostly insensitive to the flow condition and gas type, except for the nonequilibrium effects on Δ^0 and on q^0 when the wall is non-catalytic where mild resistance to changes in freestream conicity is observed.

The freestream conicity is also found to alter the normalized distributions of the shock stand-off distance Δ/Δ^0, heat flux q/q^0, surface pressure p_s/p_s^0, and boundary layer thickness δ/δ^0 with the angle from the stagnation point θ. In general, increasing the freestream conicity magnifies the slope of these distributions. For Δ/Δ^0 and δ/δ^0, which increases with increasing θ, the freestream conicity increases the gradient of the distribution curve while for q/q^0 and p_s/p_s^0, which decreases with increasing θ, the freestream conicity decreases the gradient of the distribution curve. The influence of freestream conicity on these normalized distributions is severe when $d = 4$, and appropriate corrections are likely required in most cases. When $\theta \lessapprox 40$, the results are mostly independent of the flow condition and gas type, and good agreement with analytical results is found allowing for easy corrections for the freestream conicity. However, for larger values of θ, the dependence on the flow condition and gas type shows up, and the analytical methods fail to give a reasonable prediction, thus, numerical methods will have to be used for corrections in this case.

When examining the entire flowfield, freestream conicity is found to change the gasdynamics (increase velocity, decrease temperature, pressure, and density) in such a way that a nonequilibrium flow becomes generally more frozen, thermally and chemically, throughout the flowfield. This increases the mass fraction distribution through a frozen boundary layer due to the swallowing of the inviscid flow with varying O_2 mass fraction.

Regarding the influence of freestream conicity on the boundary layer transition, an analysis is carried out using the available empirical corrections which employ the boundary layer edge conditions and the momentum thickness. It is found that if transition occurs in a uniform freestream, it would also occur in a conical freestream, albeit with the transition point shifted upstream closer to the stagnation point by about $\approx 20\%$ when $d = 4$ irrespective of the flow condition and gas state. The increase in the boundary layer edge tangential velocity caused by the freestream conicity increasing the tangential velocity gradient is found to be responsible for this upstream shift in the transition location.

Overall, at and near the stagnation point ($\theta \lessapprox 40$), the influence of freestream conicity is mostly insensitive to the flow condition and gas state, except for some special nonequilibrium effects which are only mild. Considering PG air and EQ air are essentially different types of gas with totally different species compositions, the current results are consistent with past results for some properties of the flow over a sphere which indicated a lack of dependency on the type of gas and whether the gas is in equilibrium or frozen, and this trend is extended here to more properties such as the boundary layer thickness and transition. Consequently, although the current work explicitly used variants of air as the test gas, most of the current results would apply to other types of gas too at a wide range of hypersonic flow conditions.

Acknowledgements. The experimental data presented in section 3 was acquired during the first author's employment as a postdoc under Emeritus Professor Herbert Olivier at RWTH Aachen University. The first author would also like to acknowledge Emeritus Professor Hans G. Hornung of California Institute of Technology and undergraduate student Mr Jershon Ang of The Hong Kong Polytechnic University for fruitful discussions.

Funding. This research received no specific grant from any funding agency, commercial or not-for-profit sectors.

Declaration of interests. The authors report no conflict of interest.

Data availability statement. The data that support the findings of this study are available within the article.

Author ORCIDs. S. Gu, https://orcid.org/0000-0003-3872-7355; C. Wen, http://orcid.org/0000-0002-1181-8786; J. Hao, http://orcid.org/0000-0002-8571-4728; W. Wang, https://orcid.org/0009-0004-7556-211X; Q. Wang, https://orcid.org/0000-0002-0084-9819

REFERENCES

van Albada, G.D., van Leer, B. & Roberts Jr, W.W. 1997 *A comparative study of computational methods in cosmic gas dynamics*, pp. 95–103. Berlin, Heidelberg: Springer.

Anderson, J.D. 2019 *Hypersonic and High-Temperature Gas Dynamics*. Reston, Virginia: American Institute of Aeronautics and Astronautics.

Billig, F.S. 1967 Shock-wave shapes around spherical-and cylindrical-nosed bodies. *Journal of Spacecraft and Rockets* **4** (6), 822–823.

Candler, Graham, Barnhardt, Michael, Drayna, Travis, Nompelis, Ioannis, Peterson, David & Subbareddy, Pramod 2007 Unstructured grid approaches for accurate aeroheating simulations. *AIAA Paper 2007-3959* .

Candler, Graham V 2018 Nonequilibrium hypersonic flows and hypersonic nozzle flow modeling. *Tech. Rep.* STO-AVT-352-VKI. NATO STO Lecture Series: Flow Characterization and Modeling of Hypersonic Wind Tunnels.

Capriati, M., Cortesi, A., Magin, T.E. & Congedo, P.M. 2022 Stagnation point heat flux characterization under numerical error and boundary conditions uncertainty. *European Journal of Mechanics-B/Fluids* **95**, 221–230.

Chan, W., Jacobs, P.A., Smart, M.K., Grieve, S., Craddock, C.S. & Doherty, L.J. 2018 Aerodynamic design of nozzles with uniform outflow for hypervelocity ground-test facilities. *Journal of Propulsion and Power* **34** (6), 1467–1478.

Chernyi, G.G 1961 *Introduction to Hypersonic Flow*. Academic Press.

Chue, RSM, Bakos, RJ, Tsai, C-Y & Betti, A 2003 Design of a shock-free expansion tunnel nozzle in hypulse. *Shock Waves* **13** (4), 261–270.

Collen, Peter L, Satchell, Matthew, Di Mare, Luca & McGilvray, Matthew 2022 The influence of shock speed variation on radiation and thermochemistry experiments in shock tubes. *Journal of Fluid Mechanics* **948**, A51.

Crittenden, PE & Balachandar, S 2018 The impact of the form of the euler equations for radial flow in cylindrical and spherical coordinates on numerical conservation and accuracy. *Shock Waves* **28** (4), 653–682.

Deepak, NR, Gai, SL & Neely, AJ 2012 High-enthalpy flow over a rearward-facing step–a computational study. *Journal of Fluid Mechanics* **695**, 405–438.

Di Giovanni, A. & Stemmer, C. 2018 Cross-flow-type breakdown induced by distributed roughness in the boundary layer of a hypersonic capsule configuration. *Journal of Fluid Mechanics* **856**, 470–503.

Einfeldt, B. 1988 On godunov-type methods for gas dynamics. *SIAM Journal on Numerical Analysis* **25** (2), 294–318.

Eitelberg, G, Krek, R & Beck, W 1996 Stagnation point heat transfer testing in non-equilibrium flow produced by the HEG. *AIAA Paper 1996-4504* .

Eremeitsev, IG & Pilyugin, NN 1981 Convective heating of a blunt-nosed body in a nonuniform hypersonic gas stream. *Fluid Dynamics* **16** (4), 592–597.

Eremeitsev, IG & Pilyugin, NN 1984 Friction and heat transfer in laminar and turbulent boundary layers on axisymmetric bodies in nonuniform supersonic flows. *Fluid Dynamics* **19** (2), 227–234.

Ewenz Rocher, M., Hermann, T., McGilvray, M. & Gollan, R. 2021 Correlation for species concentration on a hypersonic stagnation point with mass injection. *AIAA Journal* pp. 1–12.

Fahy, Elise J, Buttsworth, David R, Gollan, Rowan J, Jacobs, Peter A, Morgan, Richard G & James, Christopher M 2021 Experimental and computational fluid dynamics study of hayabusa reentry peak heating. *Journal of Spacecraft and Rockets* **58** (6), 1833–1846.

Farokhi, S. 2021 *Aircraft Propulsion*, 3rd edn. USA: John Wiley and Sons.

Fay, J.A. & Riddell, F.R. 1958 Theory of stagnation point heat transfer in dissociated air. *Journal of the Aerospace Sciences* **25** (2), 73–85.

Finch, Peter M, Girard, Julian J, Schwartz, Tal, Strand, Christopher L, Hanson, Ronald K, Yu, Wesley M, Austin, Joanna M & Hornung, Hans G 2023 Measurements of t5 shock tunnel freestream temperature, velocity, and composition. *AIAA Journal* **61** (4), 1555–1578.

Gibbons, N.N., Damm, K.A., Jacobs, P.A. & Gollan, R.J. 2023 Eilmer: an open-source multi-physics hypersonic flow solver. *Computer Physics Communications* **282**, 108551.

Gollan, R. & Jacobs, P.A. 2013 About the formulation, verification and validation of the hypersonic flow solver eilmer. *International Journal for Numerical Methods in Fluids* **73** (1), 19–57.

Golovachev, Yu P & Leont'eva, NV 1983 Viscous shock layer on the surface of a blunt body in a diverging supersonic flow. *Fluid Dynamics* **18** (3), 491–494.

Golovachov, Y.P. 1985 Similarity properties in the problem of flow from a supersonic source past a spherical bluntness. *International Journal of Heat and Mass Transfer* **28** (6), 1165–1171.

Goodwin, David G., Moffat, Harry K., Schoegl, Ingmar, Speth, Raymond L. & Weber, Bryan W. 2023 Cantera: An object-oriented software toolkit for chemical kinetics, thermodynamics, and transport processes. https://www.cantera.org, version 3.0.0.

Goulard, R 1958 On catalytic recombination rates in hypersonic stagnation heat transfer. *Journal of Jet Propulsion* **28** (11), 737–745.

Grossir, G, Dias, B, Chazot, O & Magin, TE 2018 High temperature and thermal non-equilibrium effects on the determination of free-stream flow properties in hypersonic wind tunnels. *Physics of Fluids* **30** (12).

Gu, S. & Olivier, H. 2020 Capabilities and limitations of existing hypersonic facilities. *Progress in Aerospace Sciences* **113**, 100607.

Gu, S., Olivier, H., Wen, C., Hao, J. & Wang, Q. 2022 Characterization of reflected shock tunnel air conditions using a simple method. *Physics of Fluids* **34** (5), 056103.

Guo, Jinghui, Wang, Xiaoyong & Li, Sijia 2024 Investigation of high enthalpy thermochemical nonequilibrium flow over spheres. *Physics of Fluids* **36** (1).

Gupta, R.N., Yos, J.M., Thompson, R.A. & Lee, K-P 1990 A review of reaction rates and thermodynamic and transport properties for an 11-species air model for chemical and thermal nonequilibrium calculations to 30000 k. *Tech. Rep.* NASA-RP-1232. NASA Tech. Mem.

Gülhan, A., Esser, B., Koch, U., Fischer, M., Magens, E. & Hannemann, V. 2018 Characterization of high-enthalpy-flow environment for ablation material tests using advanced diagnostics. *AIAA Journal* **56** (3), 1072–1084.

Hall, G.J. & Russo, A.L. 1966 Recent studies of nonequilibrium flows at the Cornell Aeronautical Laboratory. *Tech. Rep.* NASA-CR-74170. NASA Tech. Mem.

Hannemann, K., Martinez Schramm, J., Wagner, A. & Ponchio Camillo, G. 2018 The high enthalpy shock tunnel Göttingen of the German aerospace center (DLR). *Journal of Large-Scale Research Facilities* **4** (A133), 1–14.

Hein, S., Theiss, A., Di Giovanni, A., Stemmer, C., Schilden, T., Schröder, W., Paredes, P., Choudhari, M.M., Li, F. & Reshotko, E. 2019 Numerical investigation of roughness effects on transition on spherical capsules. *Journal of Spacecraft and Rockets* **56** (2), 388–404.

Hornung, HG 2010 Deriving features of reacting hypersonic flow from gradients at a curved shock. *AIAA journal* **48** (2), 287–296.

Hornung, H.G. 2019 Effect of conical free stream on shock stand-off distance. *AIAA Journal* **57** (9), 4115–4116.

Inger, George R 1963 Nonequilibrium stagnation point boundary layers with arbitrary surface catalycity. *AIAA Journal* **1** (8), 1776–1784.

Inouye, M. 1966 Numerical solutions for blunt axisymmetric bodies in a supersonic spherical source flow. *Tech. Rep.* NASA-TN-D-3383. NASA Tech. Mem.

Jacobs, PA, Gollan, RJ, Denman, AJ, O'Flaherty, BT, Potter, DF, Petrie-Repar, PJ & Johnston, IA 2010 Eilmer's theory book: basic models for gas dynamics and thermochemistry. *Tech. Rep.* Department of Mechanical Engineering Report 2010/09. The University of Queensland.

Jacobs, PA, Gollan, RJ, Jahn, Ingo & Potter, DF 2015 The eilmer3 code: User guide and example book. Report Mechanical Engineering Report 2015/07. The University of Queensland.

Jans, Elijah, Lynch, Kyle P, Wagnild, Ross, Swain, Will E, Downing, Charley, Kearney, Sean P, Wagner, Justin L, Gilvey, Jonathan J & Goldenstein, Christopher S 2024 Laser-based characterization of reflected shock tunnel freestream velocity and multi-species thermal nonequilibrium with comparison to modeling. *AIAA Paper 2024-1753* .

Karl, S., Martinez Schramm, J. & Hannemann, K. 2003 High enthalpy cylinder flow in HEG: A basis for CFD validation. *AIAA Paper 2003-4252* .

Kitamura, K., Shima, E., Nakamura, Y. & Roe, P.L. 2010 Evaluation of euler fluxes for hypersonic heating computations. *AIAA Journal* **48** (4), 763–776.

Krishna, Y., Sheehe, S.L. & O'Byrne, S. 2018 Detection of spatial variation in hypersonic nozzle flow using diode laser spectroscopy. *AIAA Journal* **56** (7), 2930–2935.

van Leer, B. 1979 Towards the ultimate conservative difference scheme. V. A second-order sequel to Godunov's method. *Journal of Computational Physics* **32** (1), 101–136.

Lees, L. 1956 Laminar heat transfer over blunt-nosed bodies at hypersonic flight speeds. *Journal of Jet Propulsion* **26** (4), 259–269.

Lin, T.C., Reeves, B.L. & Siegelman, D. 1977 Blunt-body problem in nonuniform flowfields. *AIAA Journal* **15** (8), 1130–1137.

Lobb, R.K. 1964 *Experimental measurement of shock detachment distance on spheres fired in air at hypervelocities*, , vol. 68, book section 26, pp. 519–527. Elsevier.

Lunev, V.V. & Khramov, N.E. 1970 Flow in vicinity of blunt body stagnation point in diverging hypersonic stream. *Fluid Dynamics* **5** (3), 444–447.

Luo, Kai, Wang, Qiu, Li, Jinping, Zhao, Wei & Gu, Sangdi 2023 A quasi-one-dimensional model for the stagnation streamline in hypersonic magnetohydrodynamic flows. *Physics of Fluids* **35** (3).

Lynch, K.P., Grasser, T., Spillers, R., Downing, C., Daniel, K.A., Jans, E.R., Kearney, S., Morreale, B.J., Wagnild, R. & Wagner, J.L. 2023 Design and characterization of the sandia free-piston reflected shock tunnel. *Shock Waves* pp. 1–16.

Mallinson, S.G., Gai, S.L. & Mudford, N.R. March 1996 An experimental investigation of hypervelocity flow in a conical nozzle. *Applied Scientific Research* **57**, 81–93.

Marineau, E. & Hornung, H.G. 2009 High-enthalpy nonequilibrium nozzle flow of air: experiments and computations. *AIAA Paper 2009-4216* .

Mazaheri, A. & Kleb, B. 2007 Exploring hypersonic, unstructured-grid issues through structured grids. *AIAA Paper 2007-4462* .

Menees, G.P. 1972 Experimental study of wall boundary layer growth in the 10 deg half angle conical nozzle of a reflected shock tunnel. *Tech. Rep.* NASA-TM-X-2647. NASA Tech. Mem.

Miller, C.G. 1977 Expansion tunnel performance with and without an electromagneticallyopened tertiary diaphragm. *AIAA Journal* **15** (7), 1045–1047.

Millikan, Roger C & White, Donald R 1963 Systematics of vibrational relaxation. *The Journal of Chemical Physics* **39** (12), 3209–3213.

Murzinov, I.N. 1966 Laminar boundary layer on a sphere in hypersonic flow of equilibrium dissociating air. *Fluid Dynamics* **1** (2), 131–133.

Nel, Lara, Skews, Beric & Naidoo, Kavendra 2015 Schlieren techniques for the visualization of an expansion fan/shock wave interaction. *Journal of Visualization* **18**, 469–479.

Nishikawa, Hiroaki & Kitamura, Keiichi 2008 Very simple, carbuncle-free, boundary-layer-resolving, rotated-hybrid riemann solvers. *Journal of Computational Physics* **227** (4), 2560–2581.

Olivier, H. 1995 Influence of the velocity gradient on the stagnation point heating in hypersonic flow. *Shock Waves* **5** (4), 205–216.

Oran, E.S. & Boris, J.P. 2001 *Numerical Simulation of Reactive Flow*, 2nd edn., , vol. 2. Cambridge: Cambridge University Press.

Papadopoulos, P., Venkatapathy, E., Prabhu, D., Loomis, M.P. & Olynick, D. 1999 Current grid-generation strategies and future requirements in hypersonic vehicle design, analysis and testing. *Applied Mathematical Modelling* **23** (9), 705–735.

Paredes, P., Choudhari, M.M. & Li, F. 2017 Blunt-body paradox and transient growth on a hypersonic spherical forebody. *Physical Review Fluids* **2** (5), 053903.

Paredes, P., Choudhari, M.M. & Li, F. 2018 Blunt-body paradox and improved application of transient-growth framework. *AIAA Journal* **56** (7), 2604–2614.

Park, C. 1993 Review of chemical-kinetic problems of future nasa missions. i-earth entries. *Journal of Thermophysics and Heat Transfer* **7** (3), 385–398.

Park, G., Gai, S.L. & Neely, A.J. 2016 Base flow of circular cylinder at hypersonic speeds. *AIAA Journal* **54** (2), 458–468.

Park, S-H, Neeb, D., Plyushchev, G., Leyland, P. & Gülhan, A. 2021 A study on heat flux predictions for re-entry flight analysis. *Acta Astronautica* **187**, 271–280.

Passiatore, Donatella, Sciacovelli, Luca, Cinnella, Paola & Pascazio, G 2022 Thermochemical non-equilibrium effects in turbulent hypersonic boundary layers. *Journal of Fluid Mechanics* **941**, A21.

Petzold, L.R. 1986 Order results for implicit runge–kutta methods applied to differential/algebraic systems. *SIAM Journal on Numerical Analysis* **23** (4), 837–852.

Ren, X., Yuan, J., He, B., Zhang, M. & Cai, G. 2019 Grid criteria for numerical simulation of hypersonic aerothermodynamics in transition regime. *Journal of Fluid Mechanics* **881**, 585–601.

Roe, P.L. 1981 Approximate riemann solvers, parameter vectors, and difference schemes. *Journal of Computational Physics* **43** (2), 357–372.

Rose, P.H. & Stark, W.I. 1958 Stagnation point heat-transfer measurements in dissociated air. *Journal of the Aerospace Sciences* **25** (2), 86–97.

Schilden, T., Pogorelov, A., Herff, S. & Schröder, W. 2020 Microroughness-induced disturbances in supersonic blunt body flow. *Physical Review Fluids* **5** (6), 063903.

Schrijer, F.F.J. & Bannink, W.J. 2010 Description and flow assessment of the delft hypersonic ludwieg tube. *Journal of Spacecraft and Rockets* **47** (1), 125–133.

Shapiro, E.G. 1975 Similarity properties with the flow of supersonic uniform and nonuniform flows of gas around a sphere. *Fluid Dynamics* **10** (1), 69–72.

Shen, J., Shao, Z., Ji, F., Chen, X., Lu, H. & Ma, H. 2023 High enthalpy non-equilibrium expansion effects in turbulent flow of the conical nozzle. *Aerospace* **10** (5), 455.

Sudhiesh Kumar, C. & Reddy, K.P.J. 2016 Experiments in hand-operated, hypersonic shock tunnel facility. *Shock Waves* **26** (6), 845–849.

Tanno, H. & Itoh, K. 2018 Flow characterization and current technical research issues of the HIEST hypersonic facility. *Tech. Rep.* STO-EN-AVT-325. NATO.

Van Dyke, Milton D 1958 The supersonic blunt-body problem-review and extension. *Journal of the Aerospace Sciences* **25** (8), 485–496.

Voronkin, VG & Geraskina, LK 1969 Nonequilibrium laminar boundary layer of dissociating air on axisymmetric bodies. *Fluid Dynamics* **4** (3), 99–102.

Wang, Zhihui, Bao, Lin & Tong, Binggang 2010 Rarefaction criterion and non-fourier heat transfer in hypersonic rarefied flows. *Physics of Fluids* **22** (12).

Wen, C-Y & Hornung, HG 1995 Non-equilibrium dissociating flow over spheres. *Journal of Fluid Mechanics* **299**, 389–405.

Yang, Y. & Park, G. 2019 Analysis of catalytic heat transfer for a multi-species gas mixture. *International Journal of Heat and Mass Transfer* **137**, 1088–1102.

Zander, F., Gollan, R.J., Jacobs, P.A. & Morgan, R.G. 2014 Hypervelocity shock standoff on spheres in air. *Shock Waves* **24** (2), 171–178.

Zeitoun, D., Boccaccio, E., Druguet, M.C. & Imbert, M. 1994 Reactive and viscous flow in hypersonic nozzles. *AIAA Journal* **32** (2), 333–340.

Zhao, W., Jiang, Z.L., Saito, T., Lin, J.M., Yu, H.R. & Takayama, K. 2005 Performance of a detonation driven shock tunnel. *Shock Waves* **14**, 53–59.